Anul XLVI **2001**

S T U D I A
UNIVERSITATIS BABEŞ-BOLYAI
PHYSICA

2

EDITORIAL OFFICE: Gh. Bilaşcu no. 24, 3400 Cluj-Napoca ✦ Phone 064-40.53.52

SUMAR - SOMMAIRE - CONTENTS - INHALT

STUDIA UNIVERSITATIS BABEŞ-BOLYAI, PHYSICA, XLVI, 2, 2001

EPR STUDY OF A TRINUCLEAR Mn^{II} CLUSTER ENCAPSULATED IN ONE HETEROPOLYANION

C. CRĂCIUN[1], L. DAVID[1], V. CHIŞ[1], O. COZAR[1]

ABSTRACT. The $Na_{12}[Mn_3(H_2O)_3(BiW_9O_{33})_2]\cdot 43H_2O$ complex was investigated by EPR and HF-EPR spectroscopy. The three Mn^{II} ions are antiferromagnetically coupled, the coupling constant ($J = -2.074$ cm^{-1}) being obtained from the temperature dependence of the linewidths of the signals in the 5-85 K temperature range. The S = 7/2 spin state is populated at T = 5 K and characterized by the isotropic g = 2.0 factor, the axial $D = -0.381$ cm^{-1} and rhombic $E = 0.054$ cm^{-1} zero field splitting parameters. X band EPR spectra at room and liquid nitrogen temperatures ($g_1 = 2.013$, $g_2 = 4.264$) confirm the presence of Mn^{II} coupled ions.

Introduction

The study of heteropolyoxometalates (HPOM) has been continuously increased because of their antiviral, antitumoral and antibiotic activity when used in combination with β-lactam antibiotics [1]. Properties of these high dimensional molecules (structural class, composition, size, charge) determine the range in which they are biologically active. It is well known that early transition metals are involved in biological processes. HPOM have the capacity to include different transition metals in their framework, which form clusters similar with those present in proteins. During the last years, sandwich-type HPOM with clusters of manganese(II) ions have been studied for their antiviral activity. The action against viruses as HIV, MLSV (murine leukemia sarcoma virus), RSV (respiratory syncytial virus) of the $[Mn_4(H_2O)_2(P_2W_{15}O_{56})_2]^{16-}$ [2] and $Mn_4(H_2O)_2(PW_9O_{34})_2]^{10-}$ [3] heteropolyanions have been reported.

In this context some of our research focuses on the study of sandwich-type HPOM with Mn^{II} ions, for obtaining information about the coordination mode of the manganese(II) ions to the ligand and the nature of interactions (dipolar, exchange, superexchange) which act into the metallic cluster. In this paper we present the EPR and HF-EPR study of the new $Na_{12}[Mn_3(H_2O)_3(BiW_9O_{33})_2]\cdot 43H_2O$ sandwich-type complex.

[1]Babeş-Bolyai Univ., Dept. of Physics, 1 Kogalniceanu, Cluj-Napoca, 3400 Romania.

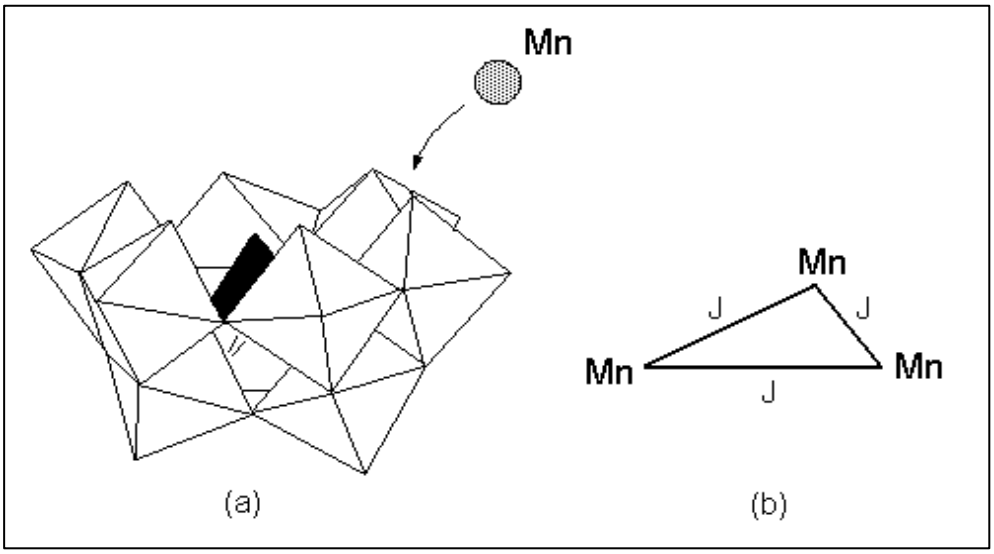

Fig.1 *(a) The α-B-$[BiW_9O_{33}]^{9-}$ heteropolyanion fragment and (b) the manganese(II) triangular cluster*

It contains two identical α-B-$[BiW_9O_{33}]^{9-}$ heteropolyanion fragments, facing each other with their open sites (Fig.1) [4]. A trinuclear manganese cluster connects the trilacunary anions. Distances greater than 4.2 Å between the Mn^{II} ions prevent the exchange interaction through direct overlapping of their orbitals. However, the manganese ions can be coupled by superexchange involving the HPOM frame or through space dipolar interactions. In analogous compound but with As^{III} as heteroatom, the Mn^{II} ions are pentacoordinated by two oxygen atoms from each trivacant Keggin unit and a water molecule in apical position. This type of coordination is also encountered for the present complex, as indicated by the FT-IR and UV-Vis studies. Geometrically, the manganese cluster is an equilateral triangle.

Experimental

EPR spectra on powdered solids have been recorded at room temperature and 80 K at *ca.* 9.6 GHz (X-band) using a Bruker ESP 380 spectrometer. W-band EPR spectra were recorded on the HF-EPR Grenoble spectrometer [5] where the 190 GHz radiation was supplied by a Gunn diode and the absorption of the millimetric waves was detected with a bolometer. Powder samples were pressed in pellets to avoid preferential orientation of the crystallites in the strong magnetic field.

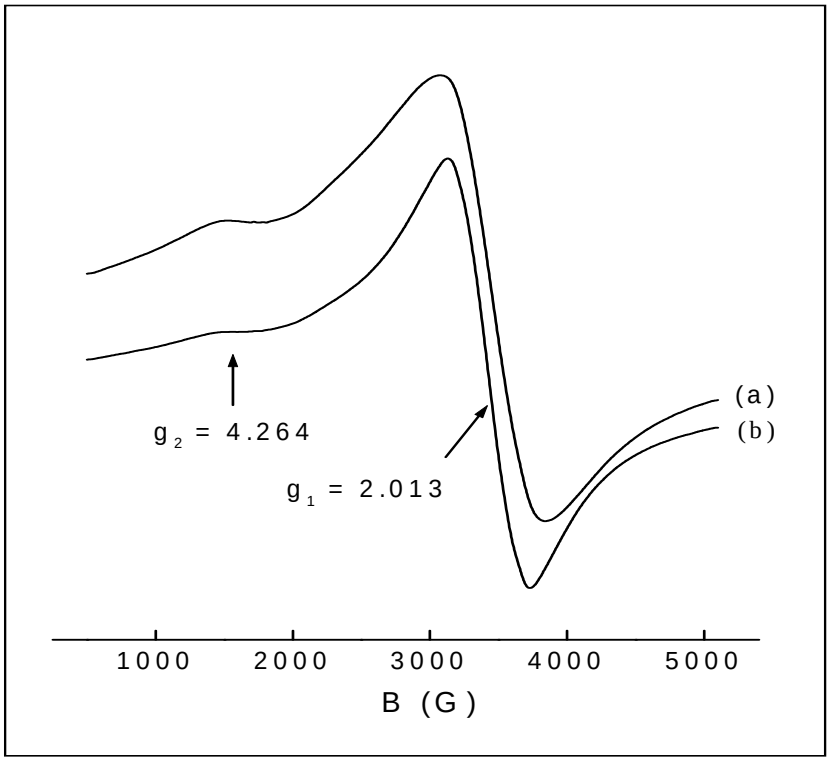

***Fig. 2**. Powder EPR spectra of the complex performed in the X band at (a) T = 80 K and (b) 293 K*

Results and discussion

Powder EPR spectra of the complex , performed in the X-band (9.6 GHz) at room and nitrogen liquid temperatures (Fig.2) contain an isotropic signal at g_1 = 2.013 typical for coupled Mn^{II} ions and another small signal at half-field (g_2 = 4.264) due to the $\Delta M_S = \pm 2$ transitions. Similar spectra have been reported for other Mn^{II} clusters, but the signals position could not say anything about the strength of the metallic coupling [6].

HF-EPR measurements have the advantage to provide information about the ground spin state of clusters with more unpaired electrons and the temperature dependence of the spectra supplies additional data about the excited states.

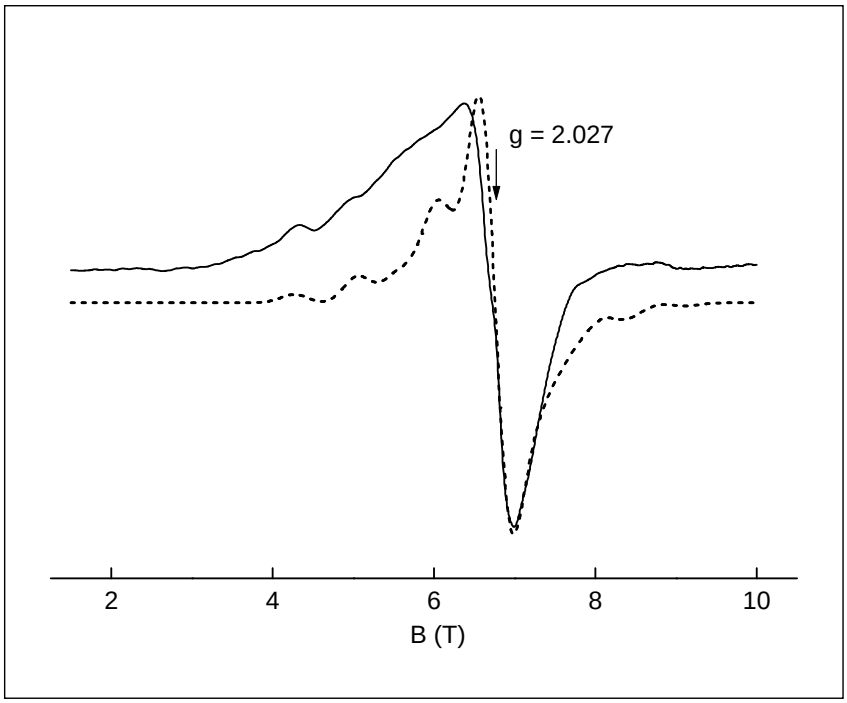

Fig.3. *The HF-EPR spectrum of a polycrystalline sample of the complex pressed in a pellet, performed at 190 GHz and T = 5 K. The pointed line represents the simulated spectrum assuming S = 7/2 spin state*

The HF-EPR spectrum of the polycrystalline sample pressed in a pellet, performed in the W-band (190 GHz) at T = 5 K temperature exhibits an asymmetric signal at about g = 2.0 (Fig.3), with two well resolved signals in the 4–5 T magnetic field region. High-spin Mn^{II} ions (S = 5/2) usually have g factors near to the g_e = 2.0023 free electron value [6]. This lead us to assign the signals at 4–5 T to the fine structure of one S = 7/2 spin state. The simulation of the spectrum (Fig.3) was made with the following EPR parameters: g = 2.027, the axial D = –0.381 cm^{-1} and rhombic E = 0.054 cm^{-1} zero field splitting and the linewidth ΔB(p-p) = 0.35 T for a Lorentzian lineshape. Although the positions of the signals in the simulated spectrum coincide with those in the experimental spectrum, the asymmetric central part of the spectrum is not very well reproduced. This is due to the EPR contribution of the lower spin states obtained by coupling antiferromagnetically the manganese ions, but there is no evidence of the fine structure arising from these states.

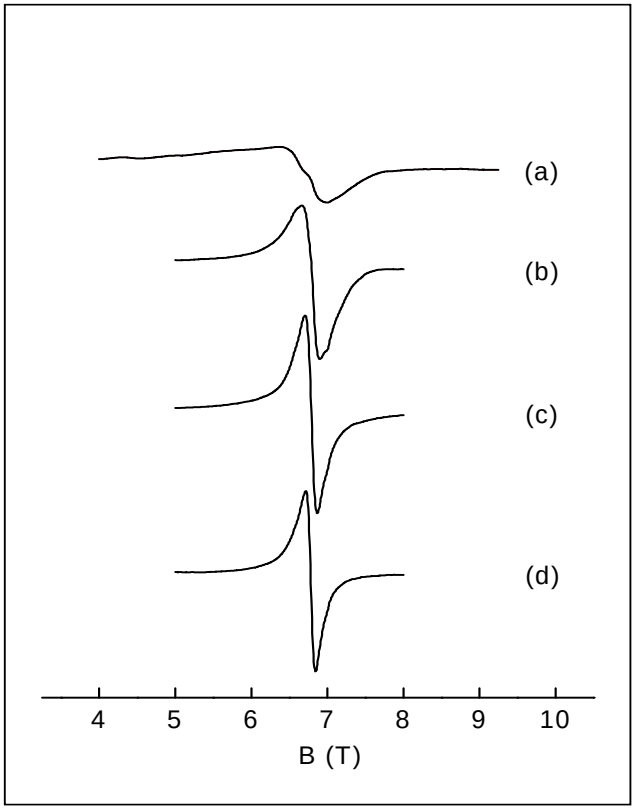

Fig.4. *HF-EPR spectra (190 GHz) of the polycrystalline complex pressed in a pellet, recorded at different temperatures: (a) 5 K, (b) 15 K, (c) 35 K, (d) 80 K*

Above T = 15 K, the HF-EPR spectrum shows a single isotropic signal centered at g ≈ 2.0 (Fig.4). The integrated intensity and the linewidth of this signal diminish by increasing the temperature, which indicates the presence of small Mn^{II}–Mn^{II} superexchange interactions. These can be described by an isotropic exchange Hamiltonian [7]:

$$H_{ex} = -J(S_1S_2 + S_2S_3 + S_1S_3) \qquad (1)$$

where J is the exchange coupling constant between the Mn^{II} ions and $\mathbf{S_1}$, $\mathbf{S_2}$ and $\mathbf{S_3}$ are the electronic spin angular momentum operators of the metallic ions which form an equilateral triangle (Fig.1b).

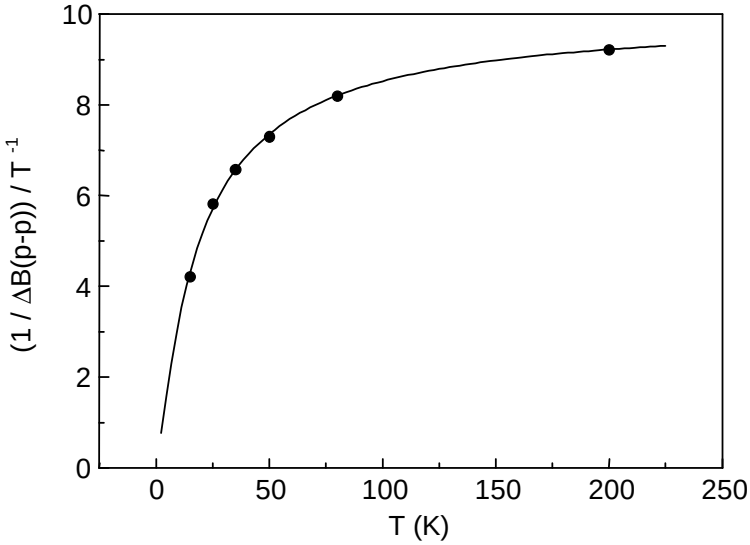

Fig.5 *Temperature dependence of the inverse of the linewidth (ΔB(p-p))$^{-1}$ of the HF-EPR signal of the complex. The solid line represents the best fit of the data.*

The temperature dependence of the inverse of the linewidth was fitted (Fig.5) taking into account the proportionality (ΔB(p-p))$^{-1}$ ~ χ_MT [8], with χ_M being the molar susceptibility in the frame of a HDVV model for three exchange-coupled high-spin Mn^{II} ions ($S_1 = S_2 = S_3 = 5/2$) [9]:

$$\chi_M T = (N\mu_B{}^2 g^2/4k)(1+20x^{3/2}+105x^4+210x^{15/2}+330x^{12}+ \\ +429x^{35/2}+455x^{24}+340x^{63/2})/(1+4x^{3/2}+9x^4+ \\ +10x^{15/2}+10x^{12}+9x^{35/2}+7x^{24}+4x^{63/2}) \qquad (2)$$

where x = exp(J/kT) and all other parameters have their usual meanings. The best fit (Fig.5) was obtained with J = –2.074 cm^{-1}, considering the g = 2.002 mean value in the 15–200 K temperature range. The negative coupling constant indicates the presence of antiferromagnetic coupled Mn^{II} ions.

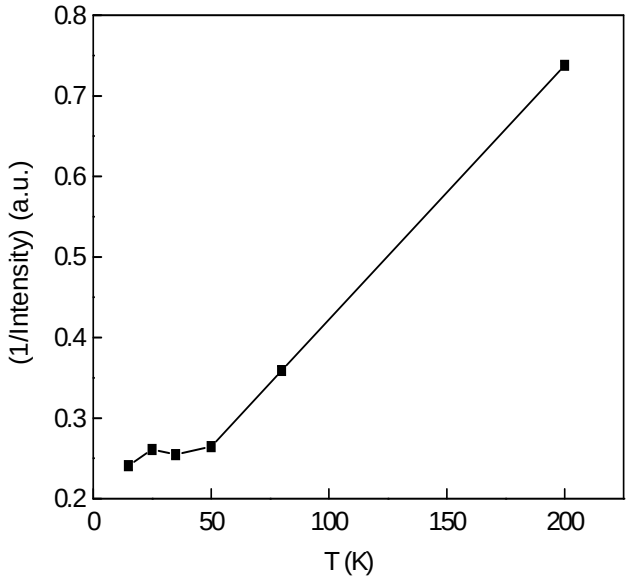

Fig.6 *Temperature dependence of the inverse of the intensity of the HF-EPR signal of the complex.*

The intensity of the signal at g ≈ 2.0 calculated by integration in the 5.3–8.3 T magnetic field range, decreases on increasing the temperature above 50 K (Fig.6). The small increase between 25–50 K (the plateau of the reciprocal intensity dependence) is probably due to antiferromagnetic intermolecular interactions [10].

Conclusion

EPR study of the $Na_{12}[Mn_3(H_2O)_3(BiW_9O_{33})_2]\cdot 43H_2O$ complex indicates the presence of coupled Mn^{II} ions. HF-EPR investigation shows that Mn^{II} ions interact antiferromagnetically. The isotropic exchange constant ($J = -2.074$ cm^{-1}) and the zero field splitting parameters ($D = -0.381$ cm^{-1}, $E = 0.054$ cm^{-1}) for the excited $S = 7/2$ state were estimated from the HF-EPR spectra of the complex obtained in the T = 5–85 temperature range. The behavior of the HF-EPR signals intensity at T < 50 K was attributed to the existence of some antiferromagnetic intermolecular interactions.

REFERENCES

1. J.T. Rhule, C.L. Hill, D.A. Judd, Chem. Rev., **98**, 327 (1998).
2. S. Shigeta, S. Mori, J. Watanabe, M. Baba, A.M. Khenkin, C.L. Hill, R.F. Schinazi, Antiviral Chem. Chemother., **6**, 114 (1995).
3. D.L. Barnard, C.L. Hill, T. Gage, J.E. Matheson, J.H. Huffman, R.W. Sidwell, M.I. Otto, R.F. Schinazi, Antiviral Res., **34**, 27 (1997).
4. B. Botar, T. Yamase, E. Ishikawa, Inorg. Chem. Comm., **3**, 579 (2000).
5. A. L. Barra, L. C. Brunel, J. B. Robert, Chem. Phys. Lett., **165**, 107 (1990).
6. D. M. L. Goodgame, M. Goodgame, P. J. Hayward, J. Chem. Soc., A, 1352 (1970).
7. A. Bencini, D. Gatteschi, in Transition Metal Chemistry, vol.8, Marcel Dekker, New York, 1982.
8. V. Tangoulis, D. A. Malamatari, K. Soulti, V. Stergiou, C. P. Raptopoulou, A. Terzis, T. A. Kabanos, D. P. Kessissoglou, Inorg. Chem., **35**, 4974 (1996).
9. P. Mialane, J. Marrot, E. Rivière, J Nebout, G. Hervé, Inorg. Chem., **40**, 44 (2001).
10. E.J. Larson, A. Haddy, M.L. Kirk, R. Sands, W.E. Hatfield, V.L. Pecoraro, J. Am. Chem. Soc., **114**, 6263 (1992).

STUDIA UNIVERSITATIS BABEŞ-BOLYAI, PHYSICA, XLVI, 2, 2001

SPECTROSCOPIC AND MAGNETIC INVESTIGATION OF ONE Cu(II) β-DIKETONATE COMPLEX

CORA CRĂCIUN[1], L. DAVID[1], V. CHIŞ[1], R. TETEAN[1]

ABSTRACT. The copper(II) β-diketonate complex CuL_2, where L = H_5C_6–CO–CH–CO–OC_2H_5 was investigated by spectroscopic (FT-IR, UV-VIS, EPR) and magnetic methods. The splitting of the ν_s(C⋯O) band from the FT-IR spectrum of the LH ligand (1576 cm^{-1}) in two bands at 1510 and 1560 cm^{-1} in the FT-IR spectrum of the complex and the coalescence of ν_{as}(C⋯O) bands which appears at 1602 and 1622 cm^{-1} for the ligand in a single red-shifted band at 1583 cm^{-1} for the complex indicate the coordination of the Cu(II) ion to the carbonyl oxygen atoms of β-diketonate molecules. The visible electronic spectrum of the CuL_2 complex contains the broad absorption bands corresponding to the $\nu(B_{1g} \rightarrow B_{2g})$ = 13075 cm^{-1} and $\nu(B_{1g} \rightarrow E_g)$ = 15410 cm^{-1} transitions for Cu(II) ion in D_{4h} local symmetry. In the UV region the intraligand π-π^* transitions (40557, 35934 and 32600 cm^{-1}) and the $L_\sigma \rightarrow M_d$ band (45567 cm^{-1}) appear. The powder EPR spectrum of the complex is rhombic, with g_1 = 2.167, g_2 = 2.082 and g_3 = 2.004. The low g values arise from the delocalization of the unpaired electron in the chelate rings and from some molecular packing effects.

Introduction

Current interest in metal β-diketonates arises from their application as contact shift reagents for better resolution of the nuclear magnetic resonance spectra of a variety of complex organic molecules, in laser technology and in the polymer industry. The coordination of the metal ions to the β-diketonates is intensively studied because of the remarkable ability to form polymeric species in the solid state and in solutions of non-coordinating solvents [1]. In this paper we report the spectroscopic and magnetic investigation of the copper(II) β-diketonate complex CuL_2, where

[1] Babeş-Bolyai Univ., Dept. of Physics, 1 Kogălniceanu, Cluj-Napoca, 3400 Romania

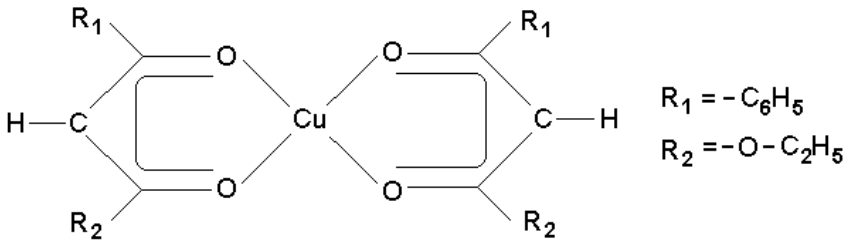

Fig.1. *The structure of the Cu(II) β-diketonate complex*

L = H_5C_6–CO–CH–CO–OC_2H_5 (Fig.1) in order to obtain information about the metallic ion coordination to the ligand, the local symmetry around the metallic center and the evidence of possible intermolecular interactions.

Experimental

The complex was prepared as previously reported [2]. FT-IR spectra were recorded on Equinox 55 Bruker Spectrophotometer on KBr pellets, in the 4000–400 cm^{-1} range. Electronic spectra were performed in aqueous solutions within a range of λ = 200–800 nm using an ATI Unicam-UV-Visible Vision Software V 3.20. EPR measurements were performed at room temperature in the X band (9.4 GHz) using a standard JEOL-JES-3B equipment. The magnetic susceptibility measurements were obtained on a Faraday type balance in the temperature range of 100–290 K.

Results and discussion

FT-IR Spectra

FTIR spectrum of the ligand (Fig.2a) indicates the coexistence of the ketonic and enolic tautomeric structures for the sample of LH = H_3C–CO–CH_2–CO–CH_3 β-diketonate ligand, because of the presence of the vibrations ν_{as}(C···O) at 1602, 1622 cm^{-1} (ketonic form), ν(C=O) at 1681, 1738 cm^{-1} and ν(O–H) at 3335 cm^{-1} (enolic form) [3-6]. After the Cu(II) coordination to the β-diketonate ligand, the ketonic form disappears [1,7]. This coordination corresponds to the increase of the quasi-aromatic behavior of the β-diketonate ring. The direct consequence is the lowering of the $\nu_{s,as}$(C···O) stretching modes for the metallic complex comparative to the β-diketonate [7] (Table 1).

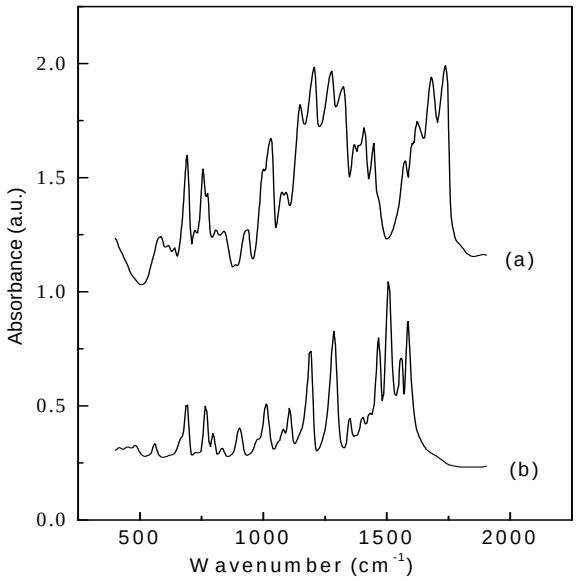

Fig.2. *FT-IR spectra of (a) the LH ligand and (b) the Cu(II) β-diketonate complex*

Table 1. Some FT-IR data (cm^{-1}) of the β-diketonate ligand and the corresponding Cu(II)-complex

Band	LH	CuL_2
$\nu_{as}(C\cdots C)+ \nu_{as}(C–CH_3)$	1277 s,sp	1287 s,sp
$\delta(C–H)+ \nu_{as}(C\cdots C)$	1325 s,sp 1368 m,sp	1348 w,sp
$\nu(C\cdots O)+\delta(C–H)$	1410 m,sp	1404 w,sp 1430 w,sp
$\nu_s(C\cdots C)$	1448 m,sp	1468 s,sp
$\nu_s(C\cdots O)$	1576 m,sp	1510 vs,sp 1560 s,sp
$\nu_{as}(C\cdots O)$	1602 m,sp 1622 m,b	1575 vs,sp 1583 s,sp

s-strong, vs-very strong, m-medium, w-weak,
sh-shoulder, b-broad, sp-sharp

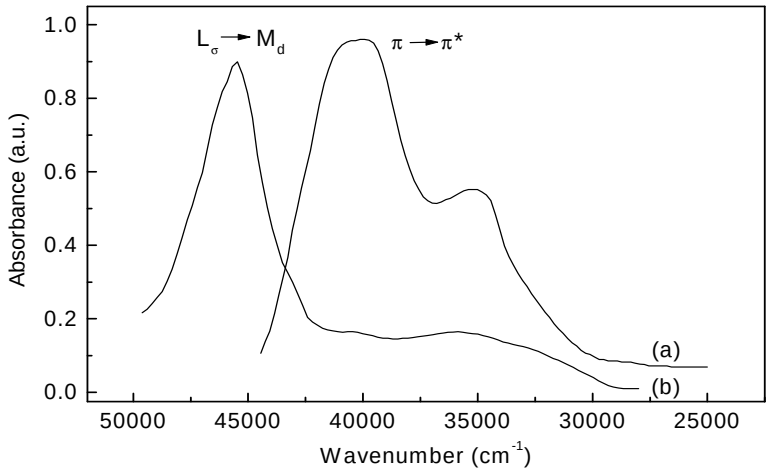

Fig.3.*UV spectra of the (a) β-diketonate ligand and (b) Cu(II)-complex, in 5·10^{-5} mol·l^{-1} aqueous solution*

The two C⋯O bonds are nonequivalent in the ligand but equivalent for the Cu(II) complex.

UV-VIS Spectra

The UV spectrum of the β-diketonate ligand (Fig.3) contains the intraligand π-π* transitions at 40244 cm^{-1} and 35176 cm^{-1} [1].

These bands are shifted towards higher energy in the Cu(II)-complex (40557 cm^{-1}, 35934 cm^{-1}), but a supplementary band appears at 32600 cm^{-1} (Fig.3). In addition, the complex spectrum contains the ligand-to-metal charge transfer $L_\sigma \rightarrow M_d$ situated at 45567 cm^{-1}, a proof of the Cu(II) coordination to the ligand. In the VIS region of the complex spectrum (Fig.4) two bands are obtained for the Cu(II) ion in D_{4h} local symmetry: $\nu(B_{1g} \rightarrow B_{2g})$ = 13075 cm^{-1} and $\nu(B_{1g} \rightarrow E_g)$ = 15410 cm^{-1} [8].

EPR Spectra

Experimental powder EPR spectrum of the CuL_2 complex, obtained at room temperature (Fig.5), was simulated with g_1 = 2.167, g_2 = 2.082 and g_3 = 2.004 principal values of the **g** tensor and $\Delta B_1 = \Delta B_2 = \Delta B_3$ = 40 G

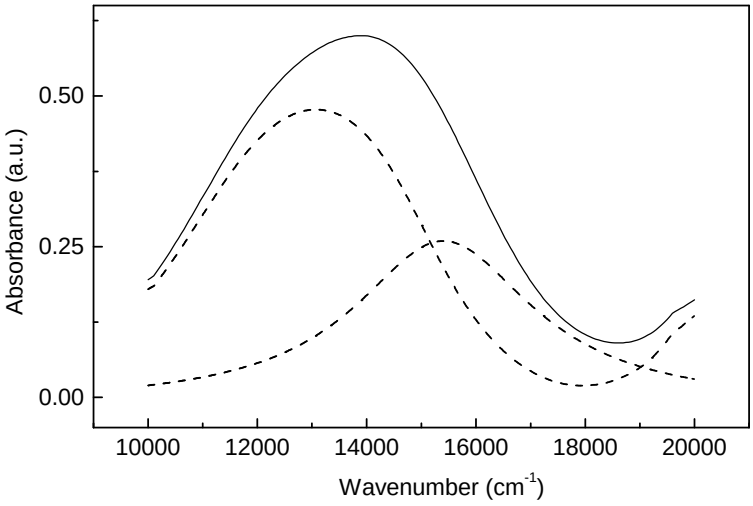

Fig.4. *VIS spectrum of the Cu(II)-complex in 10^{-3} mol·l^{-1} aqueous solution (solid line) and its components (dashed line)*

linewhidts. EPR parameters indicate the presence of one rhombic distortion of the local symmetry around the Cu(II) ion, because of the nonequivalent $-C_6H_5$ and $-O-C_2H_5$ substituents of the β-diketonate molecule. These low g values arise from the delocalization of the unpaired electron in the chelate rings and from some molecular packing effects [9,10].

Magnetic susceptibility measurements

Temperature dependence of the magnetic susceptibility data (Fig.6) was fitted by considering a Curie–Weiss behavior [11]:

$$\chi_M = \frac{N\mu_B^2\mu_{eff}^2}{3k(T-\theta)} + \chi_0$$

Diamagnetic corrections (χ_0 = $-219.46\cdot10^{-6}$ e.m.u./mol) were estimated from Pascal tables. The value of the effective moment μ_{eff} = 1.79 μ_B is typical for spin only Cu(II) ions in a square-planar environment. The negative Weiss temperature ($\theta \approx -15$ K) is a proof for the presence of antiferromagnetic intermolecular interactions.

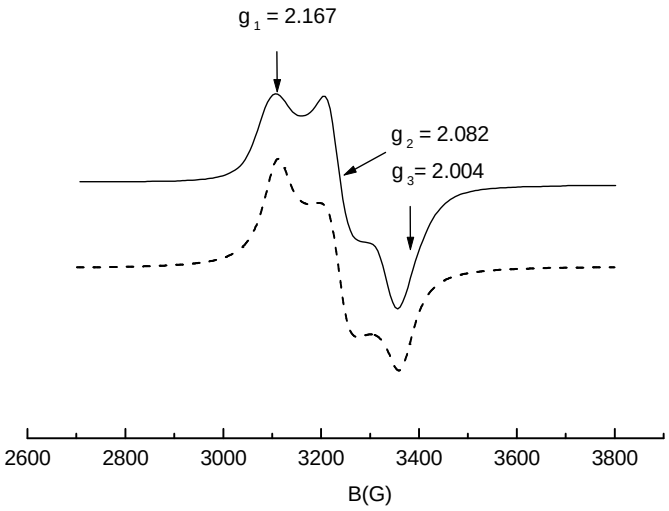

Fig. 5. Powder EPR spectrum of the Cu(II) β-diketonate complex obtained at room temperature (solid line) and its simulated spectrum (dashed line)

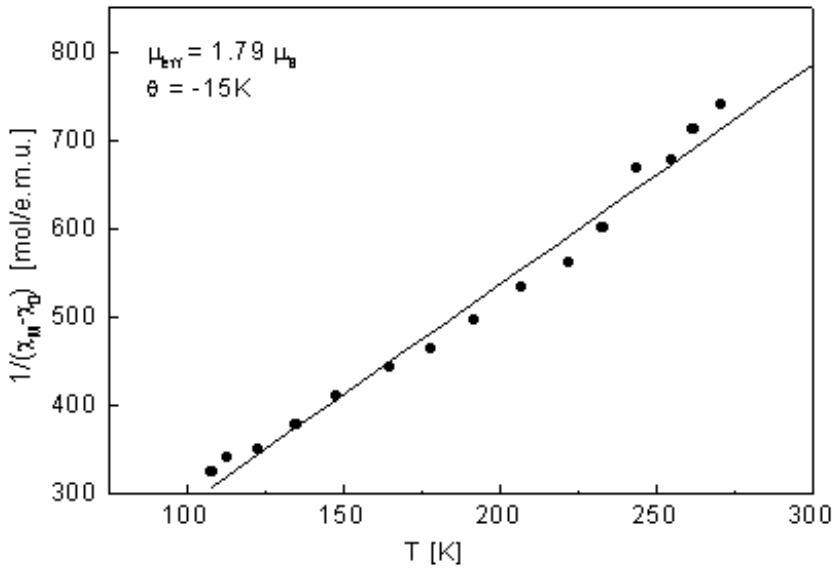

Fig. 6. *The temperature dependence of the inverse of the molar susceptibility (χ_M - χ_0). The straight line represents the best fitt of the experimental data*

Conclusions

The coordination of the Cu(II) ions to the oxygen atoms of the β-diketonate molecules is indicated by the shift of the ν(C⎓O) vibrations in the FT-IR spectrum of the complex and also by the appearance of the $L_\sigma \rightarrow M_d$ ligand-to-metal charge transfer bands in the UV region. The ketonic and enolic tautomeric structures coexist for the ligand, but only the second of them appears in the complex sample. The Cu(II) ion is coordinated by four oxygen atoms in a square-planar configuration, with a $d_{x^2-y^2}$ orbital as ground state. The local symmetry is rhombic distorted because of the nonequivalent $-C_6H_5$ and $-O-C_2H_5$ substituents of the β–diketonate molecules. The relative low principal values of the ***g*** tensor and the negative Weiss temperature indicate the presence of antiferromagnetic intermolecular interactions. This agrees with the monocrystal structure consisting of planar molecules situated in parallel planes.

REFERENCES

1. R.C. Mehrotra, R. Bohra, D.P. Gaur, Metal β-Diketonates and allied derivatives, Academic Press, London, 1978.
2. I. Baxter, S.R. Drake, M.B. Hursthouse, K.M. Abdul Malik, J. McAleese, D.J. Otway, J.C. Plakatouras, Inorg. Chem., **34**, 1384 (1995).
3. G. Schmidt, U. Behrens, Journ. of Organomet. Chem., **503**, 101 (1995).
4. R.K.Y. Ho, R.L. Martin, Aust. J. Chem., **26**, 2299 (1973).
5. O. Siiman, D.D. Titus, C.D. Cowman, J. Fresco, H.B. Gray, J. Am. Chem. Soc., **96(8)**, 2353 (1974).
6. G. Voutsas, K. Keramidas, D. Venetopoulou, C. Tsiamiss, Zeitscrift für Kristallographie, **210**, 100 (1995).
7. K. Nakamoto, Infrared Spectra of Inorganic and Coordination Compounds, 2nd. Ed. John Wiley & Sons, New York, 1970.
8. A.B.P. Lever, Inorganic Electronic Spectroscopy, 2nd. Ed. Elsevier, New York, 1984.
9. S.A. Chizhanov, V.I. Volkov, A.V. Vorobiev, V.V. Valuev, Russ. J. of Phys. Chem., **7**, 67 (1993).
10. G. Plesch, C. Friebel, O. Svajlenova, J. Kratesmar-Smogrovic, D. Mlynarcik, Inorg. Chim. Acta, **151**, 139 (1988).
11. F.E. Mabbs, D.J. Machin, Magnetism and Transition Metal Complexes, John Wiley & Sons Ed., New York, 1973.

STUDIA UNIVERSITATIS BABEŞ-BOLYAI, PHYSICA, XLVI, 2, 2001

EPR AND MAGNETIC SUSCEPTIBILITY DATA ON $MnO-B_2O_3-As_2O_3$ GLASSES

I. ARDELEAN, M . PETEANU, R. CICEO-LUCACEL, P. PASCUTA, M. FLORA*

Faculty of Physics, Babes-Bolyai University, 3400 Cluj-Napoca, Romania
**Faculty of Science, University of Oradea, 3700 Oradea, Romania*

ABSTRACT. Glasses of the $xMnO\cdot(100-x)[2B_2O_3\cdot As_2O_3]$ system were investigated by means of EPR and magnetic susceptibility measurements, within $0 < x \leq 50$ mol % MnO. The valence states of manganese ions, their distribution in the host matrix and the interactions implying them, were revealed in function of concentration. Structural details of the vitreous system were also evidenced at different doping levels.

Introduction

There are several aspects of the EPR absorption spectra due to paramagnetic ions in vitreous matrices which recommend them as valuable in revealing the structural details of the diamagnetic host, the coordination and valence state of the paramagnetic probes. Manganese ions gave information about the structural properties of number of oxide glasses such as borate [1-6], alkalisilicate [7], phosphate [8, 9], tellurite [10-12] and also chalcogenide [13] or halide [14, 15] glasses.

The magnetic behaviour of manganese ions was also studied in potassium- [4], lead- [16], lithium- [17], cadmium- [6] borate and also in tellurite [12], bismuthate [18] and lead-bismuthate [19, 20] oxide vitreous matrices. The type and strength of interactions involving manganese were determined in function of concentration and also the valence states of magnetic-active ions were revealed.

Glasses of the $MnO-B_2O_3-As_2O_3$ vitreous system were studied by means of EPR and magnetic susceptibility measurements. This paper aims to present the corresponding results.

Experimental

Glasses of the system $xMnO\cdot(100-x)[2B_2O_3\cdot As_2O_3]$ were prepared by using reagent grade compounds: $MnCO_3$, H_3BO_3, As_2O_3. The melting was performed in an electric furnace, using sintered corundum crucibles, at 1200^{o}C, during 30 min. The quenching at room temperature was achieved by pouring the molten material on stainless-steel plates. Typical glasses were obtained up to x = 50 mol % MnO. Their structure was tested by using X-ray diffraction analysis, selecting samples with concentrations of MnO whose patterns were typical for vitreous solids. No crystalline phases were evidenced within $0 \leq x \leq 50$ mol % MnO.

EPR absorption spectra were obtained using a SEX-201/RADIOPAN spectrometer, at room temperature, in the X-frequency band (9.3 GHz).

Magnetic susceptibility measurements were performed in the 80-300 K temperature range, using a Faraday-type translation balance.

Results

For all samples EPR absorption spectra due to paramagnetic Mn^{2+} ions were detected. Their structure depend on the MnO content of the sample (Fig.1). The signal-parameters dependence on the Mn^{2+} concentration was also followed. The estimated EPR parameters of the resonance line were the peak-to-peak width, ΔB, the line-amplitude I, and the intensity approximated by $J = I\cdot(\Delta B)^2$. The corresponding concentration-dependencies are presented in Fig. 2.

The temperature dependence of the reciprocal magnetic susceptibility of the investigated glasses is presented in Fig. 3. The composition dependencies of the molar Curie constant, C_M, and the paramagnetic Curie temperature, θp, are given in Table 1. The magnetic moments of manganese ions were estimated as $\mu_{exp} = 2.827\ (C_M/x)^{1/2}$. The obtained values of μ_{exp} for samples with x > 1 mol % MnO (Table 1) lie between those corresponding to Mn^2+ and Mn^3+ free-state ions, i.e. $\mu_{Mn^{2+}} = 5.92\ \mu_B$ and $\mu_{Mn^{3+}} = 4.90\ \mu_B$ to that both valence states are supposed to be present in the vitreous sample for $1 \leq x \leq 50$ mol % MnO.

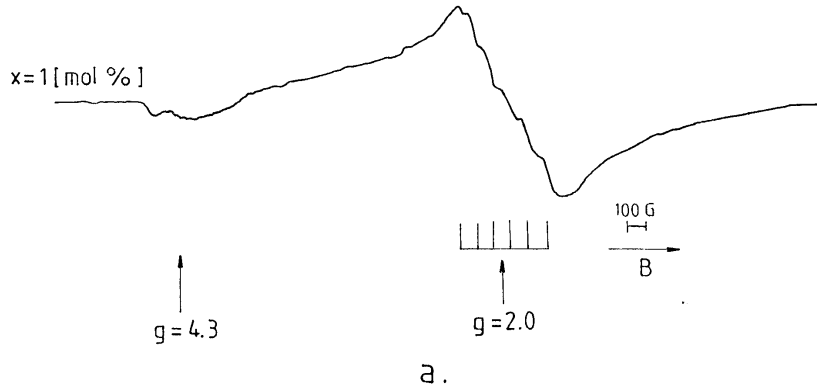

a.

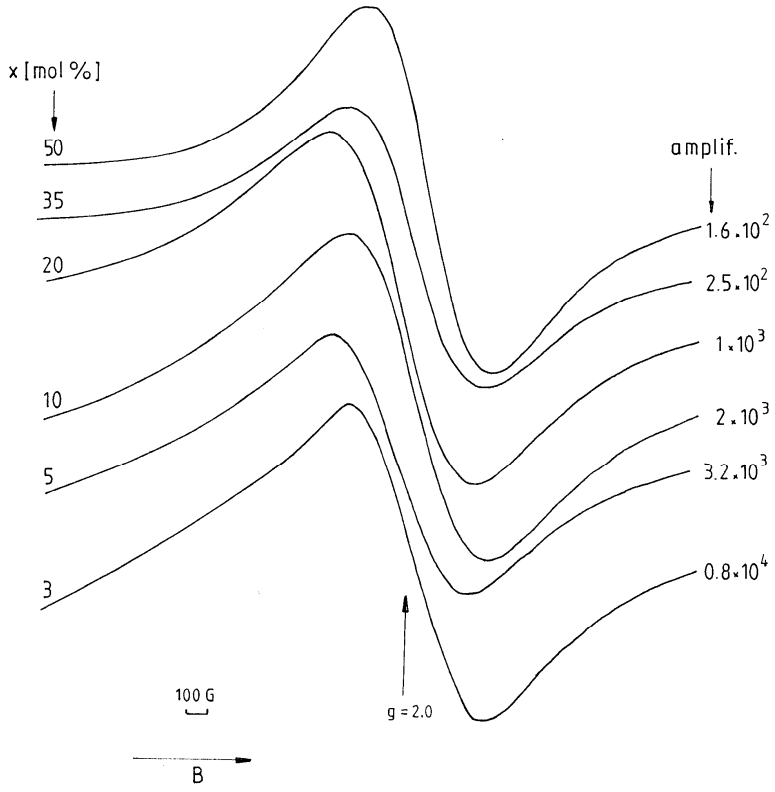

b.

Fig. 1. EPR absorption spectra due to Mn^{2+} ions in $xMnO\cdot(100-x)[2B_2O_3\cdot As_2O_3]$ glasses.

The molar fraction of manganese ions in these two possible valence states were estimated in first approximation according to

$$x\mu_{exp}^2 = x_1\mu_{Mn^{2+}}^2 + x_2\mu_{Mn^{3+}}^2 ,$$
$$x = x_1 + x_2 ,$$

where x_1 and x_2 are the molar fractions of Mn^{2+} and Mn^{3+} ions, respectively. The obtained values are given in Table 1.

Table 1

Molar Curie constants, effective magnetic moments, paramagnetic Curie temperatures and molar fractions of Mn^2+ and Mn^3+ ions in xMnO·(100-x) [$2B_2O_3$·As_2O_3] glasses.

x [mol % MnO]	C_M [e.m.u./mol] x10^2	μ_{exp} [μ_B]	θp [K]	x_1 [mol % Mn^2+O]	x_2 [mol % Mn^3+O]
1	4.39	5.92	0	1	-
3	12.83	5.84	0	2.73	0.27
5	29.90	5.76	0	4.13	0.87
10	39.35	5.60	-8	6.60	3.40
20	75.22	5.48	-22	10.74	9.26
35	123.44	5.31	-44	12.88	22.12
50	164.89	5.14	-65	10.22	39.78

Discussion

The EPR absorption spectra are due to the Mn^2+ ($3d^5$; $^6S_5/2$) ions entering the matrix as paramagnetic species. The detected spectra show the line centered at g ≈ 2.0 as the preponderant contribution to the EPR absorption (Fig. 1). At low manganese content, x ≤ 1 mol % MnO, the characteristic hyperfine structure (hfs) due to the interaction with the nuclear spin I = 5/2, was resolved. The resolution was lost with increased concentration due to the ligand field fluctuations in the Mn^2+ ion vicinity and to the dipolar interactions. The separation ΔB_{hf} between the hfs lines increases progressively in the sense of the magnetic field, suggesting second order effects to be taken into account in an accurate theoretical approach.

The absorption signals having a resolved hfs are due to isolated Mn^2+ ions in sites of octahedral symmetry poorly distorted. The strongly distorted versions of such vicinities give rise to absorption lines at g ≈ 4.3 representing the contribution to EPR of Mn^2+ ions subjected to strong

crystal field effects. The most probable structural configurations at the origin of g ≈ 4.3 signals are, in the case of manganese ions, the octahedral ones rhombically or tetragonally distorted. For the investigated glasses the g ≈ 4.3 lines were detected only at low paramagnetic ions concentration (Fig. 1). Due to their extremely low intensity comparatively to those detected at g ≈ 2.0, the lack of hfs, and their poor resolution, we may conclude the presence of manganese ions involved in the above mentioned structural units in an extremely low concentration, and also great fluctuations in the crystal field parameters values, i.e. an appreciable structural variety of the corresponding units.

Even for the Mn^{2+} ions giving rise to g ≈ 2.0 absorption lines there are appreciable crystal field parameters distributions explaining the poor resolution of hfs and its loosing when increase concentration. The line reduces to the envelope of contributions at resonance. Besides the ions structurally involved in well defined units, there are those of "uncertain" vicinity, which are no longer strictly coordinated with the surrounding oxygens, giving rise to a broad structureless line. In the previous section we pointed out the reasons for which Mn^{3+} ions also are to be taken into account when increasing the MnO content of the sample. Without giving rise to an EPR absorption, these ions interact with the Mn^{2+} ones and consequently influence their resonance line. In such circonstances manganese ions become involved in clusters of Mn^{2+} and Mn^{3+} species.

The evolution of the EPR absorption line at g ≈ 2.0 was revealed by the concentration dependence of its parameters (Fig. 2). The line-width (Fig. 2a) increases up to 5 mol % MnO due to dipol-dipol interactions. For x > 5 mol % the line narrows suggesting mechanisms of superexchange-type interaction

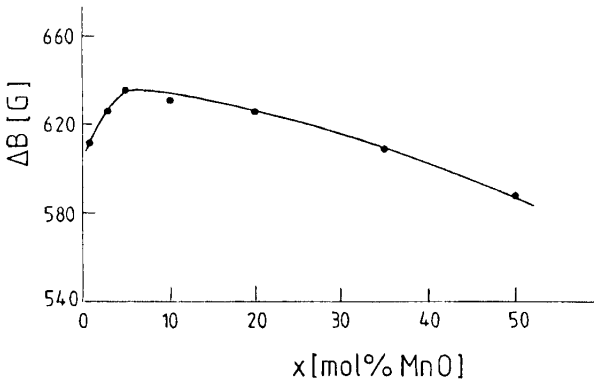

a.

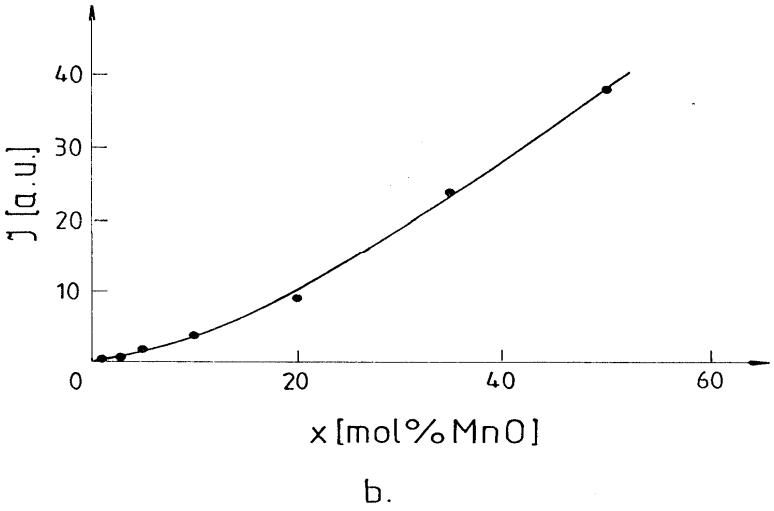

Fig. 2. Concentration dependence of the line-width (a) and the line-intensity (b) for signals at g ≈ 2.0 in the EPR absorption spectra of Mn^{2+} ions in $xMnO·(100-x)[2B_2O_3·As_2O_3]$ glasses.

between manganese ions. This assumption is confirmed by the magnetic susceptibility measurements which revealed the change in the temperature dependence of the reciprocal magnetic susceptibility from a Curie-type behaviour characteristic to isolated ions or involved in dipolar interactions, to a Curie-Weiss-type one, specific to antiferromagnetically coupled ions by means of superexchange interactions (Fig. 3). This changement was evidenced at concentrations of about 5 mol % MnO. The concentration dependence of the paramagnetic Curie temperature (***Table 1***) show an increasing of the θp absolute value for x > 5 mol % MnO reflecting the increasing of magnetic interactions with the increased number of involved manganese ions. This narrowing mechanism is balanced by the broadening ones, especially by the Mn^{2+}-Mn^{3+} dipolar interaction inside the clusters, and consequently the line-width decreasing for x > 5 mol % MnO in Fig. 2a is not very pronounced. According to Table 1 the Mn^{3+} ions content is appreciable in samples with x > 20 mol % MnO. According to magnetic data, it results that for x ≤ 1 mol % concentrations only Mn^{2+} ions are present in the studied glasses.

The line-intensity evolution revealed in Fig. 2b suggests the clustering tendencies of manganese ions more pronounced for x ≥ 5 mol % MnO. The absorption line intensity increases progressively with the MnO content in the sample, especially for x > 5 mol % when passing from

samples containing preponderantly isolated Mn2+ ions to those were ionic clusters are prevalent.

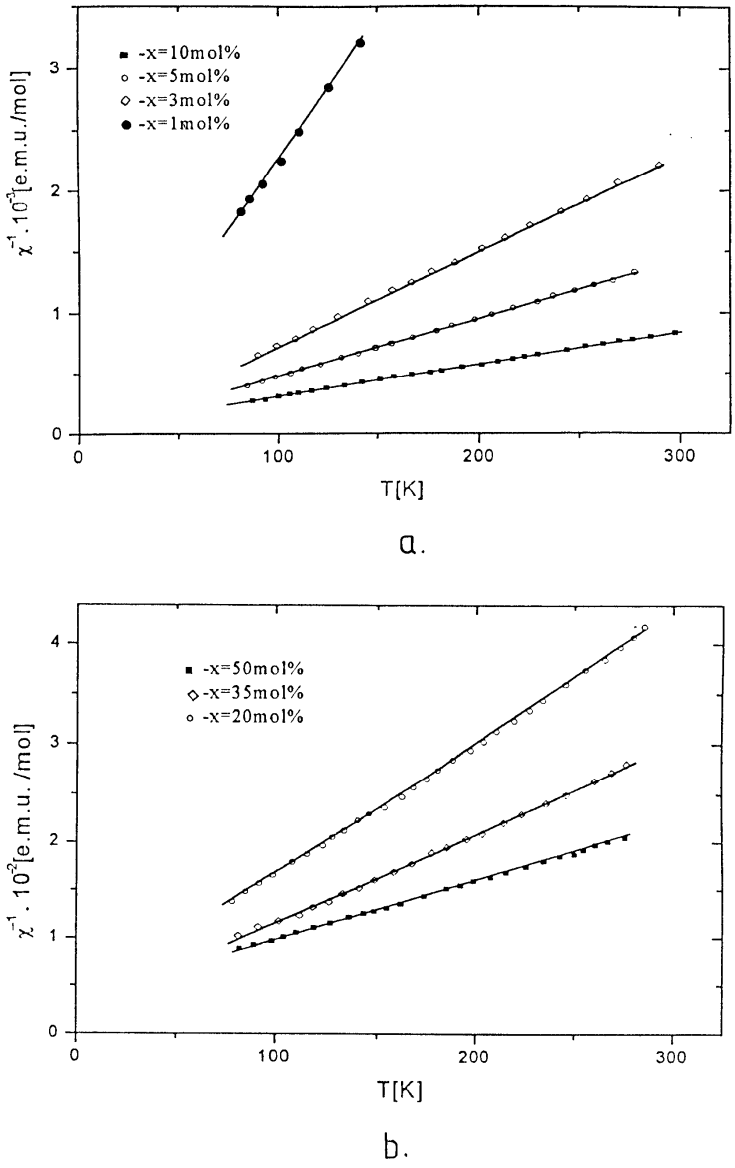

Fig. 3. Temperature dependence of the reciprocal magnetic susceptibility of some representative glasses of the system xMnO·(100-x)[$2B_2O_3$·As_2O_3] for 1 ≤x ≤10 mol % (a) and 20 ≤x ≤50 mol % (b) concentration range.

Conclusions

Homogeneous glasses of the $xMnO\cdot(100-x)[2B_2O_3\cdot As_2O_3]$ system were obtained within $0 \leq x \leq 50$ mol % MnO.

EPR absorption spectra due to Mn^{2+} ($3d^5$; $6S^{5/2}$) were obtained for all concentrations. The Mn^{3+} valence state was also detected for samples with $x > 1$ mol % MnO by means of magnetic susceptibility measurements. Both valence states coexist for $1 < x \leq 50$ mol % the molar fraction of Mn^{3+} ions exceeding that of Mn^{2+} ions for $x > 20$ mol % MnO.

Up to 1 mol % Mn^{2+} ions enters the matrix involved in low-symmetric structural units subjected to strong crystal field effects, resulting in $g \approx 4.3$ resonance lines. The high symmetric versions of structural units involving Mn^{2+} give rise to the $g \approx 2.0$ lines showing a resolved hfs. The matrix is not structurally stable when MnO accumulates in the sample, so the concentration range of isolated Mn^{2+} in well defined structural units is relatively short and hfs rapidly smears out.

Broaden unresolved lines at $g \approx 2.0$ due to clusters of ions show manganese as agglomerated in disordered vicinities for $x > 5$ mol % MnO. For such compositions magnetic susceptibility data evidenced manganese ions as experience negative magnetic interactions and predominantly antiferromagnetic coupling. The superexchange mechanisms narrow the EPR resonance lines at $g \approx 2.0$ but this narrowing is balanced by Mn^{2+}-Mn^{3+} interactions.

REFERENCES

1. D.L.Griscom, R.E.Griscom, J. Chem. Phys. 47, 2711 (1967).
2. R.D.Dowsing, J.F.Gibson, J. Chem. Phys. 50, 294 (1989).
3. P.C.Taylor, P.J.Bray, J. Chem. Phys. Solids 52, 147 (1972).
4. I.Ardelean, Gh.Ilonca, M.Peteanu, Solid State Commun. 52, 147 (1984).
5. I.Ardelean, M.Peteanu, V.Simon, S.Filip, M.Flora, S.Simon, J. Mat. Sci. 34, 6063 (1999).
6. I.Ardelean, M.Peteanu, V.Simon, S.Simon, M.Flora, Phys. Chem. Glasses 41 (3), 153 (2000).
7. D.Loveridge, S.Parke, Phys. Chem. Glasses 12, 19 (1971).
8. J.W.Schreurs, J. Chem. Phys. 69, 215 (1973).
9. I.Ardelean, M.Peteanu, O.Cozar, V.Simon, V.Mih, G.Botezan, J. Mat. Sci. Technol. 15(5), 453 (1999).

10. M.Peteanu, I.Ardelean, Al.Nicula, Rev. Roum. Phys. 28, 147 (1983).
11. I.Ardelean, M.Peteanu, Gh.Ilonca, Phys. Stat. Sol. (a), 58, K33 (1983).
12. M.Peteanu, I.Ardelean, S.Filip, D.Alexandru, Rom. Journ. Phys. 41, 593 (1996).
13. J.V.Chepeleva, E.A.Zhilinskaja, V.N.Lazukin, A.P.Cernov, V.J.Olkhovskij, Phys. Stat. Sol. (b) 82, 189 (1977).
14. B.Petrova, M.Frumar, E.Cernoskova, V.Cerny, J. Non-Cryst. Solids 161, 316 (1993).
15. V.Cerny, B.Frumarova-Petrova, J.Rosa, I.L.Licholit, M.Frumar, J. Non-Cryst. Solids 192-193, 165 (1995).
16. Gh.Ilonca, I.Ardelean, O.Cozar, J. Physique 49, 8 (1988).
17. I.Ardelean, Gh.Ilonca, O.Cozar, Rev. Roum. Phys. 33, 179 (1988).
18. I.Ardelean, M.Peteanu, S.Filip, V.Simon, I.Todor, Solid State Commun. 105, 334 (1998).
19. I.Ardelean, S.Simon, M.Peteanu, V.Simon, F.Ciorcas, C.Bob, Mat. Letters 39, 42 (1999).
20. I.Ardelean, M.Peteanu, S.Simon, V.Simon, F.Ciorcas, C.Bob, S.Filip, Indian J. Phys. 74A(5), 467 (2000).

STUDIA UNIVERSITATIS BABEŞ-BOLYAI, PHYSICA, XLVI, 2, 2001

MAGNETIC BEHAVIOUR OF OXIDE LEAD-BISMUTHATE GLASSES CONTAINING IRON IONS

R. POP[a], V. SIMON[b], I. COSMA[c], M. COLDEA[b]

[a] *University of Civil Engineering, Physics Department, Bucharest, Romania*
[b] *Babes-Bolyai University, Faculty of Physics, 3400 Cluj-Napoca, Romania*
[c] *Technical University, Physics Department, 3400 Cluj-Napoca, Romania*

ABSTRACT. The investigated samples belong to the $xFe_2O_3(100-x)[3Bi_2O_3 \cdot 2PbO]$ system ($1 \leq x \leq 20$ mol %) and were obtained by melting the suitable mixtures at 1100 ^{0}C for ten minutes in air, followed by fast undercooling to room temperature. The magnetic susceptibility, measured with a Faraday-type magnetic balance, may be described with a Curie – Weiss law for $5 \leq x \leq 20$ mol % Fe_2O_3 and with a Curie-type law for x = 1mol % Fe_2O_3. Negative paramagnetic Curie temperatures have been found suggesting the antiferromagnetic nature of the magnetic interaction between the Fe ions in the studied samples. According to the magnetic moment values, calculated from the experimental data, the valence state of the Fe ions is changing from Fe^{3+} to Fe^{2+} as the concentration x increases from 1 to 20 mol % Fe_2O_3. The ratio Fe^{2+} / Fe^{3+} was determined for each sample.

1. Introduction

The heavy metal glasses have attracted considerable attention due to their interesting physical properties (high density, high polarisability, long infrared cut-off, high non-linear optical susceptibility) leading to different applications like radiation shielding windows, scintillation counters, optical transmission devices, ultrafast optical switches [1-4]. It is known that many Bi-based glass systems are converted into high-T_c superconductors after appropriate annealing [5].

Furthermore, many glasses containing transition metal oxides have semiconducting properties. In this kind of glasses the electron conductivity is due to a thermally activated hopping process of d electrons between ions in different valence states [6]. The presence of both ions Fe^{2+} and Fe^{3+} was pointed out in many glasses with Fe_2O_3 [7-12].

The aim of this paper is to study the magnetic properties of the $xFe_2O_3(100\text{-}x)[3Bi_2O_3 \cdot 2PbO]$ glasses and finally to determine the magnetic state of Fe ions and the nature of magnetic interactions in these systems and how the magnetic state of Fe ions is changing with the concentration of the Fe_2O_3 oxide. An attractive reason in studying these glasses consists also in the fact that they do not contain any conventional glass former such as SiO_2, B_2O_3, P_2O_5, GeO_2, etc.

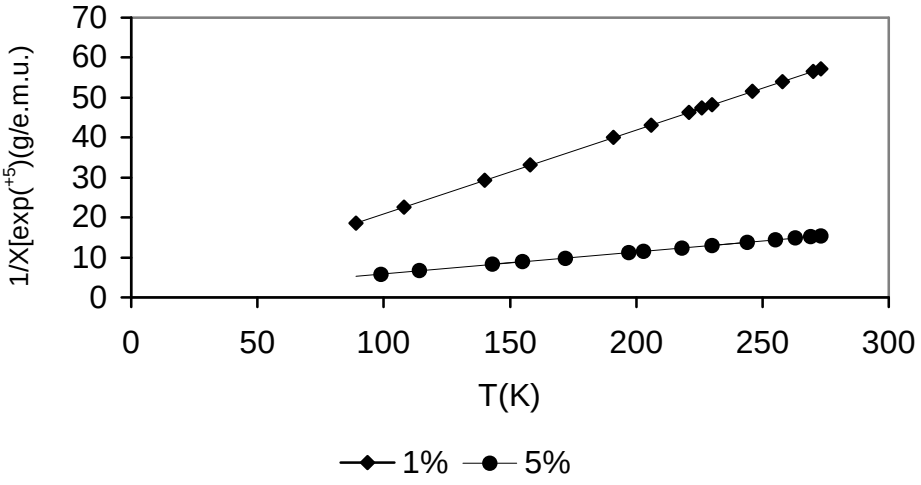

Fig. 1 . The reciprocal susceptibility versus temperature for x =1 mol % and 5 mol % Fe_2O_3.

2. Experimental

The starting materials used to prepare the samples were analytically pure reagents $(BiO)_2CO_3$, PbO and Fe_2O_3. The suitable mixtures were melted in sintercorundum crucibles in an electric furnace, in air, at 1100 ^{0}C for 10 minutes. The melts were subsequently quenced between two stainless steel plates at room temperature. The glass state in the system Bi_2O_3 – PbO can be obtained only at high cooling rates.

The X – ray diffraction patterns of the investigated samples, with x = 1 ; 5 ; 10 and 20 mol % Fe_2O_3, consist in broad lines typical for disordered systems.

The magnetic susceptibility was measured between 80K and 300K with a 10^{-8} emu/g sensitivity Faraday-type magnetic balance. Corrections for the diamagnetism of sample holder and of the ion cores were applied.

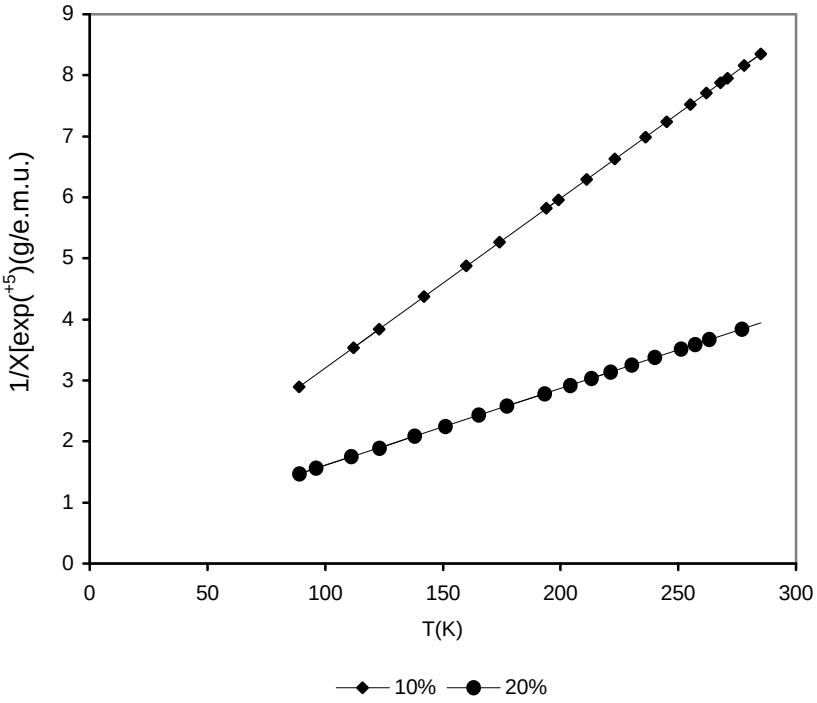

Fig. 2 . The reciprocal susceptibility versus temperature for x =10 mol % and 20 mol % Fe_2O_3.

3. Results and discussion

Figures 1 and 2 show the temperature dependence of the reciprocal susceptibility of the $xFe_2O_3(100\text{-}x)[3Bi_2O_3{\cdot}2PbO]$ glasses for x = 1 ; 5 ; 10 and 20 mol %. The magnetic susceptibility for x = 1 mol % verifies the Curie law $\chi = C / T$, suggesting that the Fe ions are isolated and do not interact by a superexchange mechanism via the oxygen ions. This was expected due to the small concentration of the Fe_2O_3 oxide in this sample. For the other three samples with higher Fe_2O_3 concentration, the magnetic

susceptibility obeys a Curie – Weiss law, $\chi = C / (T - \Theta_p)$, with a negative intercept at the paramagnetic Curie temperature Θ_p.

In Table 1 are given the values of the Curie constants, the magnetic moments per Fe ion and the paramagnetic Curie temperatures for the investigated samples. As one can see from Fig. 3, the paramagnetic Curie temperatures increases linearly with the Fe_2O_3 content. It is well known that the paramagnetic Curie temperature is an indicator of both the strength of the interaction between the magnetic moments and the number of magnetic ions participating in the interaction. The negative values of this parameter is consistent with the antiferromagnetic nature of the interaction in the investigated glasses. These magnetic interactions become stronger at the higher Fe_2O_3 concentration.

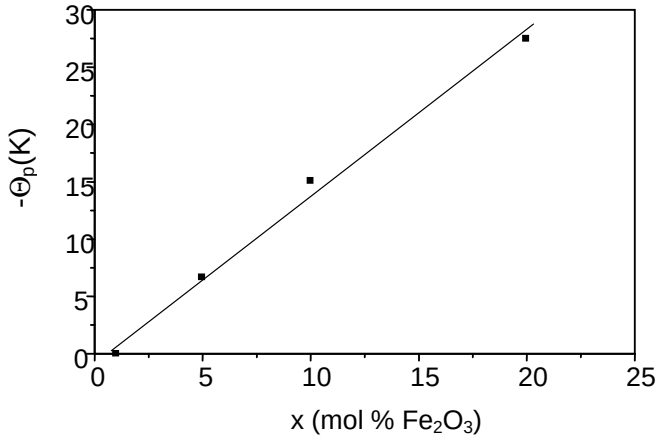

Fig. 3. Paramagnetic Curie temperature versus Fe_2O_3 content.

Table 1

Magnetic moments per Fe ion, paramagnetic Curie temperatures and the Curie constants for the $xFe_2O_3(100-x)[3Bi_2O_3 \cdot 2PbO]$ glasses

x	Magnetic moment (μ_B/Fe)	$-\Theta_P$(K)	C_M(K·emu/mol)
1	5,91	0	0,08722
5	5,02	6,7	0,3147
10	4,91	15,1	0,602
20	4,90	27,4	1,194

The magnetic moment per Fe ion decreases as the Fe_2O_3 increases. The value of the magnetic moment per Fe ion in the sample with x = 1 mol % is very close to the theoretical value $5.90\mu_B$ (for the $3d^5$ configuration, S = 5/2), showing that in this glass all the Fe ions are in the Fe^{3+} valence state as in the Fe_2O_3 oxide. On the other hand, the magnetic moment per Fe ion in the samples with x = 10 and 20 mol % are very close to the value $4.90\mu_B$ of the free Fe^{2+} ion ($3d^6$ configuration, S = 2). For the intermediate concentration x = 5 mol %, the value of the magnetic moment is between these two limits. This means that in this sample both Fe^{2+} and Fe^{3+} ions are present. The molar fraction of Fe^{2+} and Fe^{3+} ions can be estimated using the relations

$$x\cdot\mu_{exp}^2 = x_1\cdot\mu^2_{Fe^{2+}} + x_2\cdot\mu^2_{Fe^{3+}}$$
$$x = x_1 + x_2,$$

where $\mu_{exp} = 2.83(C_M/2x)^{1/2}$ is the experimental effective magnetic moment per unit formula and x_1 and x_2 are the molar fraction of the iron ion in the Fe^{2+} and respectively Fe^{3+} valence states. The obtained values for this glass are as follows : x_1 = 4. 46 and x_2 = 0.54.

4. Conclusions

Summarizing the results one may conclude that the magnetic state of Fe ions in the heavy glasses $xFe_2O_3(100\text{-}x)[3Bi_2O_3\cdot 2PbO]$ changes from Fe^{3+} for x = 1 mol % to Fe^{2+} for x = 10 and 20 mol % Fe_2O_3, while for x = 5 mol % both ions are present. The magnetic interactions between Fe ions are of antiferromagnetic origin, the coupling increasing with the Fe_2O_3 content.

REFERENCES

1. A. A. Karmalov, R. M. Almeida, J.Heo, J. Non-Cryst. Solids, 202, 233 (1996).
2. J. Fu, H. Yatsuda, Phys. Chem. Glasses, 36, 211 (1995).
3. Y. B. Dimitriev, V. T. Mihailova, J. Mater. Sci. Lett., 9, 1251 (1990).
4. W. H. Dumbaugh, J. C. Lapp, J. Am. Ceram. Soc., 75, 2315 (1992).
5. T. Komatsu, R. Sato, K. Imai, K. Matusita, T. Yamashita, Jap. Apll. Phys., 27, 550 (1998).
6. E. Agostinelli, P. Filaci, D. Fiorani, A. Montenero, M. Bettinelli, J. Non-Cryst. Solids, 84, 329 (1986).

7. B. Kumar, C. H. Chen, J. Appl. Phys., 75, 6760 (1994).
8. I. Ardelean, Gh. Ilonca, O. Cozar, V.Simon, S. Filip, Mat. Letters, 21, 321 (1994).
9. I. Ardelean, M. Peteanu, S. Filip, V. Simon, G. Györffy, Solid State Commun., 102, 341, (1997).
10. B. Kumar, C. H. Chen, S. Liu, Phys. Chem. Glasses, 38, 45 (1992).
11. A. Mekki, D. Holland, C. F. McConville, M. Salim, J. Non-Cryst. Solids, 208, 267, (1996).
12. A. Mekki, Phys. Stat. Sol.(a), 184, 327 (2001).

STUDIA UNIVERSITATIS BABEŞ-BOLYAI, PHYSICA, XLVI, 2, 2001

THERMAL DIFFUSIVITY STUDY ON IRON CONTAINING CaO-P_2O_5-SiO_2 GLASSES AND GLASS CERAMICS

V. SIMON*, D. DADARLAT, A. PASCA**, S. SIMON***

**Babes-Bolyai University, Faculty of Physics, 3400 Cluj-Napoca, Romania*
***National Institute for Research and Development of Isotopic and Molecular Technologies, 3400 Cluj-Napoca, Romania*
****Lucian Blaga University, Physics Department, 2400 Sibiu, Romania*

ABSTRACT. Standard photopyroelectric (SPPE) measurements were carried out in order to obtain the thermal diffusivity, α, for $45(3.34\ CaO{\cdot}P_2O_5)(55\text{-}x)SiO_2{\cdot}xFe_2O_3$ glass and glass-ceramic samples with $0 \le x \le 30$ mol %. The room temperature values of the thermal diffusivity in the above mentioned composition range are $0.41{\cdot}10^{-6} \le \alpha \le 2.33{\cdot}10^{-6}$ m^2/s. Vitroceramic samples obtained by heat treatment present a similar behaviour of the thermal diffusivity with that of the untreated samples. The temperature dependence $\alpha(T)$ in the range of interest ($10 \div 65^oC$) indicates a linear decrease of α with a slope of 10^{-8} m^2/s /degree.

Introduction

Several studies reported in the last two decades point out that hyperthermia is a promising approach for cancer therapy [1-4]. The challenge in this method is to restrict local heating of the tumor without damaging the healthy tissues in the tumor surrounding [5]. The use of calcium phosphate ceramics and glass ceramics as bone substitutes has become common in orthopedic surgery [4, 6, 7]. Ferromagnetic calcium phosphate glass ceramics are successfully applied to reinforce the curettaged bone and to decrease the recurrence of tumors by hyperthermic treatment because the hysteresis heating raises the temperature sufficiently to induce necrosis and significant delay of tumor growth [8]. In order to realize such a treatment in the case of bone cancer are used

materials of similar compositions with the major mineral phase of the bone $Ca_{10}(PO_4)_6(OH)_2$ (hydroxyapatite) wherein the ratio Ca/P is 1.67. The glass system $CaO\text{-}P_2O_5\text{-}SiO_2\text{-}Fe_2O_3$ with the ratio Ca/P = 1.67 attracted a special interest [2, 8, 9]. For medical applications like hyperthermia are to be taken into account beside the magnetic also the thermal properties of the materials used. This is the reason why this study is devoted to thermal diffusivity measurements of $CaO\text{-}P_2O_5\text{-}SiO_2\text{-}Fe_2O_3$ system. Due to the fact the dynamic thermal parameters (e.g. thermal diffusivity) are more difficult to be measured than the static ones (e.g. specific heat), a new and performant calorimetric method (the photopyroelectric technique) has been used in this study.

Experimental

The start materials used to obtain $45(3.34\ CaO{\cdot}P_2O_5)(55\text{-}x)SiO_2{\cdot}xFe_2O_3$ glass system were $CaCO_3$, $CaHPO_4{\cdot}2H_2O$, SiO_2 and Fe_2O_3 of reagent grade purity. The oxide mixtures corresponding to the desired compositions ($0 \leq x \leq 30$ mol %) were melted in corundum crucibles at 1550^oC for 10 minutes in an electric furnace in air under normal conditions. The melts were quickly undercooled by pouring onto stainless steel plates at room temperature. The glasses were then heat treated at 1000^oC for 30 minutes and slowly cooled to room temperature in the disconnected furnace. The samples were mechanically polished as plates of thickness ranging between 620 and 780 μm with plan parallel faces.

The measurements of thermal diffusivity were performed in the standard photopyroelectric configuration (SPPE) with thermally thick sensor and sample and optically opaque sample. A typical computer controled set-up was used for investigations [10]. The PPE detection cell was a double room system, provided with Peltier elements for temperature control [10]. The pyroelectric sensor was a 300 μm thick $LiTaO_3$ monocrystal provided with metallic (Cr-Ni-Au) electrical contacts on both faces. The thermal contact between the sample and sensor was assured with a coupling fluid (silicon grease).

The samples with $x \neq 0$ are opaque with regard to the wavelength of the laser source (He-Ne, 10 mW), while the sample with $x = 0$ is slightly transparent and, therefore, it was necessary to simulate an opaque probe by gluing on its front face a 15 μm thick blackened aluminum foil. In this way one may consider that the heat source is localised in a plane situated at the sample surface. Additionally, a one directional propagation of the heat was assumed.

In order to check for the thermally thick regime of the sample and sensor, a frequency scan of the phase of PPE signal was performed . This scan allows the determination of the room temperature value of the thermal diffusivity, indicating in the same time the most suitable chopping frequency necessary for the temperature scan, in this case 1 Hz. The investigated temperature range 10 ÷ 65 ^oC encompasses the range of medical interest (42 ÷ 45 ^oC). The temperature variation rate was 0.015 $^oC/s$.

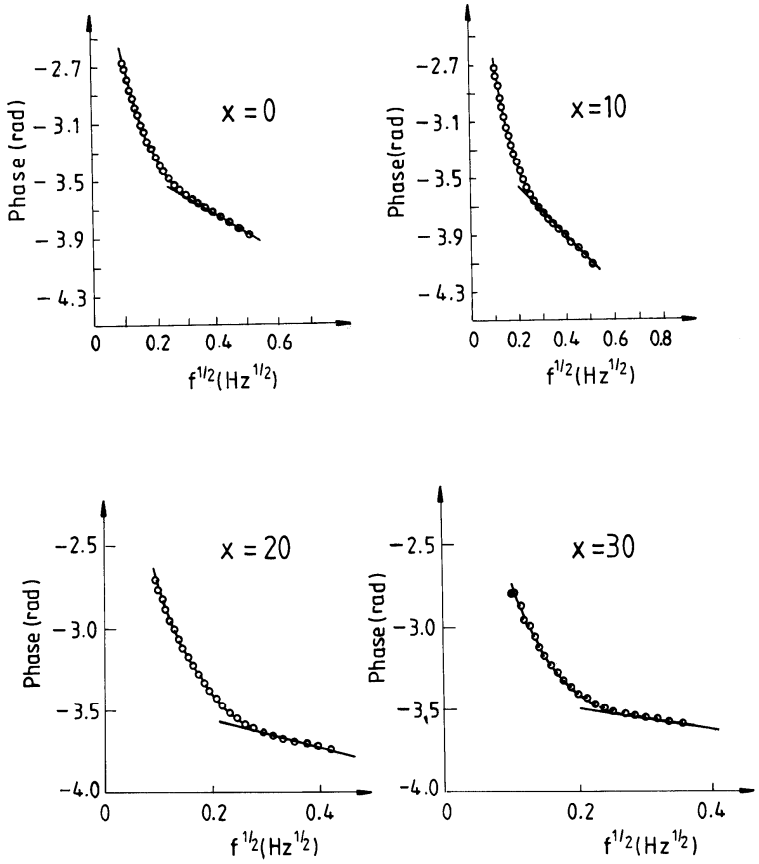

Figure 1. The phase of the PPE signal versus the square root of the modulation frequency for some 45(3.34 $CaO{\cdot}P_2O_5$)(55-x)$SiO_2{\cdot}xFe_2O_3$ samples.

Results and discussion

Due to the fact that the local atomic order and the valence state of metals in oxide matrices play an important role in determining their physical properties and implicitly their capability to aggregate in clusters [11], all these effects induced by heat treatment are to be expected also for the iron

ions contained in the investigated samples. The segregation of iron atoms in clusters is interesting from the standpoint of bioactive ferromagnetic glass ceramic materials. Having in mind the different iron containing crystalline phases development in the investigated glass system, the heat treatment conditions (1000^{o}C, 30 minutes) for partial crystallisation were established according to earlier results obtained on $CaO-P_2O_5-SiO_2-Fe_2O_3$ system [12]. The highest local concentration for iron inside the samples was obtained for the glass ceramic resulting by the treatment applied at 1000^{o}C.

At the same time, the presence of ferromagnetic phases and of a thermal diffusivity without anomalies as a function of temperature are necessary to achieve the goal of materials used for hyperthermia therapy. The room temperature values of the thermal diffusivity α, were calculated for all samples using the equation [13]:

$$\alpha = \pi \cdot L^2/S^2$$

where L is the thickness of the sample and S the slope of the linear part of the corresponding phase vs. sqrt(f) curve, as illustrated in Figure 1. The results are summarised in Table 1.

Table 1

Room temperature values for the thermal diffusivity of 45(3.34 $CaO \cdot P_2O_5$)(55-x)$SiO_2 \cdot xFe_2O_3$ glass samples.

x (mol %)	L (μm)	S ($s^{-1/2}$)	α ($10^{-6}m^2/s$)
0	735	-2.205	0.41
10	620	-1.376	0.64
20	740	-1.069	1.52
30	750	-0.877	2.33

For the sample containing the lowest content of Fe_2O_3 (x = 10 mol %) the value obtained for the thermal diffusivity is of same magnitude order like for quartz [14]. One observes an increase of thermal diffusivity by $0.41 \div 0.88 \cdot 10^{-6}$ m^2/s per mol % as Fe_2O_3 is added to the investigated $CaO-P_2O_5-SiO_2$ glass matrix. Practically there is a linear dependence α vs. x in the composition range $10 \leq x \leq 30$ mol %, as can be seen from Figure 2. The heat treatment applied in order to develop desired crystalline phases with ferromagnetic behaviour does not affect the value of thermal diffusivuty. The slopes obtained from the PPE phase dependences on the frequency square root (Fig. 3) lead to the same α value both for untreated and treated sample with thickness of 620 and 780 μm, respectively. At the same time, one remarks that thermal diffusivity for treated and untreated samples depends in a similar way on temperature (Fig. 4). The temperature

dependence $\alpha(T)$ indicates a linear decrease of 10^{-8} m^2/s /degree between 10 and 65°C. This very slight decrease shows a good stability of the thermal diffusivity in the temperature range of interest for possible hyperthermia applications.

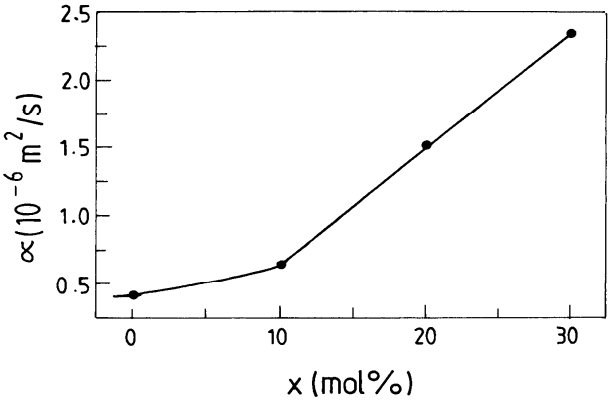

Figure 2. The composition dependence of the thermal diffusivity for 45(3.34 $CaO{\cdot}P_2O_5$)(55-x)$SiO_2{\cdot}xFe_2O_3$ glass samples

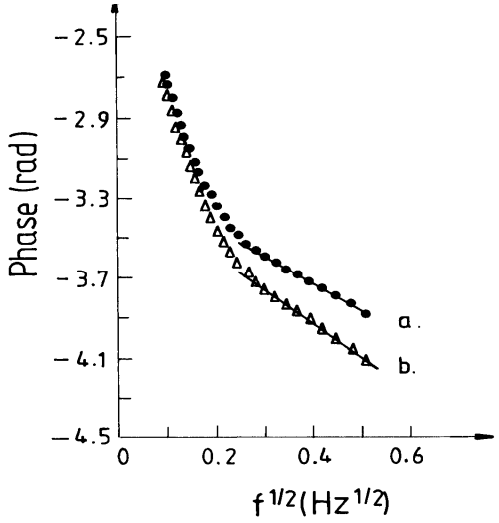

Figure 3. The phase of the PPE signal versus square root of modulation frequency for untreated (a) and heat treated (b) 45(3.34 $CaO{\cdot}P_2O_5$)45$SiO_2{\cdot}10Fe_2O_3$ sample.

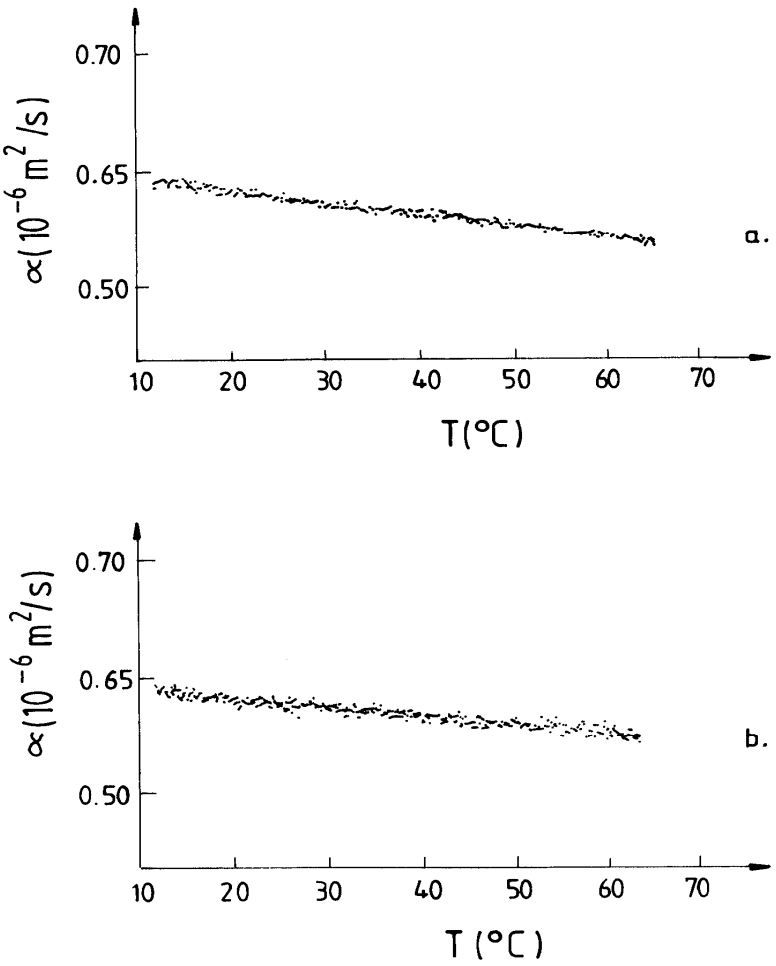

Figure 4. Temperature dependence of thermal diffusivity for untreated (a) and heat treated (b) 45(3.34 $CaO{\cdot}P_2O_5$)45$SiO_2{\cdot}10Fe_2O_3$ sample.

Conclusions

Photopyroelectric calorimetry, in standard configuration, on 45 (3.34 $CaO{\cdot}P_2O_5$)(55-x)$SiO_2{\cdot}xFe_2O_3$ glass and glass-ceramic ($0 \le x \le 30$ mol %), was used in order to calculate the room temperature value of the thermal diffusivity, α. The values obtained for the investigated composition range are $0.41{\cdot}10^{-6} \le \alpha \le 2.33{\cdot}10^{-6}$ m^2/s. The thermal diffusivity value of vitroceramic samples is the same as for the glass samples. The

temperature dependence $\alpha(T)$ indicates a linear decrease of 10^{-8} m^2/s /degree both before and after heat treatment, and denotes a good stability of the thermal diffusivity in the investigated temperature range, including the interval of interest for therapy by hyperthermia.

REFERENCES

1. A. Jordan, R. Scholz, K. Maier-Hauff, M. Johannsen, P. Wust, J. Nadobny, H. Schirra,H. Schmidt, S. Deger, S. Loening, W. Lanksch, R. Felix, J.Magn.Magn. Mater, 225, 119 (2001).
2. K. Ohura, M. Ikenaga, T. Nakamura, T. Yamamuro, M. Hiraoka, Y. Ebisawa, T. Kokubo,Y. Kotoura and M. Oka, in *Ceramics in Substitutive and Reconstructive Surgery*, P.Vincenzini (ed.), Elsevier Science Publishers, B.V., 1991.
3. M. Gautherie, *Biological Basis of Oncologic Thermotherapy*, Springer, Berlin, 1990.
4. A. Dupraz, T.P. Nguyen, M. Richard, G. Daculsi, N. Passuti, *Biomaterials*, 20, 663 (1999).
5. M. Babinkova, D. Leszczynska, P. Sourivong, P. Cicmanec, P. Babinec, J.Magn.Magn.Mater, 225, 109 (2001).
6. M. Jarcho, *Clin.Orthop.*, 157, 259 (1981).
7. R.Z. LeGeros, *Biomechanics in orthopaedics*, Springer, 1991, p.147-174.
8. K.Ohura, M.Ikenaga, T.Nakamura, T.Yamamuro, Y.Ebisawa, T.Kokubo, Y.Kotoura, M.Oka, J. Appl. Biomaterials, 2, 153 (1991).
9. M. Ikenaga, K. Ohura, T. Nakamura, Y. Kotoura, T. Yamamuro, M. Oka, Y. Ebisawa,T. Kokubo, *Bioceramics*, vol.4, eds. W. Bonfield, G.W. Hastings, K.E. Tanner, Butterworth-Heinemann, London, p.255,1991.
10. A. Pa¿ca, *Studiul efectelor fototermice în stare condensat¾*, Teza de doctorat, Univ. Babe¿-Bolyai, Cluj-Napoca, 2001.
11. F. D'Acapito, S. Mobilio, J.R. Regnard, E. Cattaruzza, F. Gonella, P. Mazzoldi, J.Non-Cryst.Solids, 232-234, 364 (1998).
12. V. Simon, S.G. Chiuzbaian, M. Neumann, D. Eniu, E. Indrea, A. Torok-Kiss, S. Simon, Mod.Phys. Lett. B., 14, 21, p. 767 (2000).
13. D. Dadarlat, K. J. Riezebos, D. Bicanic, C. van den Berg, E. Gerkema, V. Surducan, Adv. Food Sci., 20, 27-33 (1998).
14. D. Almond & A. Patel, *Phototherml Science and Techniques*, Chapman & Hall, London, 1996.

STUDIA UNIVERSITATIS BABEŞ-BOLYAI, PHYSICA, XLVI, 2, 2001

STRUCTURAL, ELECTRIC AND MAGNETIC STUDIES ON Pb_2FeNbO_6 COMPOUND

I. ARDELEAN[a], I. BARBUR[a], G. BORODI[b], D. CIOMOS[a]

[a]*Faculty of Physics, Babes-Bolyai University, 3400 Cluj-Napoca, Romania*
[b]*Institute of Isotopic and Molecular Technologies, 3400 Cluj-Napoca, Romania*

ABSTRACT. Structural, electric and magnetic measurements were performed on Pb_2FeNbO_6 (PFN). The X-ray diffraction studies indicate the absence of ordering of the ions, and PFN may be considered as a disordered solid solution. From the temperature dependence of the dielectric permitivity may be concluded that PFN exhibit a ferroelectric phase transition at 110 – 140^{o}C. At the same time, magnetic measurements confirm the antiferromagnetic behaviour of this compound.

INTRODUCTION

Lead perovskites of the general formula $Pb_2B'B''O_6$ (B': Mg, Zn, Ni, Fe, Mn; B'': W, Nb, Ta, Mo) are characterized by very good dielectric and electrostrictive properties [1] and form a large groups of compounds possessing either ferroelectric (FE) or antiferroelectric (AFE) phase transitions [2].

Pb_2FeNbO_6, hereafter designated PFN is a compound of $A_2^{2+}B^{3+}B^{5+}O_6$ type with perovskite-type structure in which the two kinds of ions (Fe^{3+} and Nb^{5+}) occupy octahedral positions.

Smolenskii et al [3] found from studies on powder samples that Pb_2FeNbO_6 might be ferroelectric with anomaly in dielectric constant at

Curie temperature of 112^{o}C. Bokov et al. [4] prepared single crystals of Pb_2FeNbO_6 and showed that the compound is ferroelectric but also appears to be an antiferromagnetic material due to the high concentration of Fe^{3+} ions in octahedral positions.

In the present work we report structural, electric and magnetic studies on PFN in polycrystalline form.

EXPERIMENTAL

The polycrystalline samples of Pb_2FeNbO_6 were prepared by reacting corresponding stoechiometric proportions of PbO, Fe_2O_3 and Nb_2O_5 species using high-purity grade chemicals. The mixture was calcined at 700^{o}C for 4 hrs and sintered at 900^{o}C for 1 h. All the samples were prepared in air atmosphere.

The X-ray diffraction measurements were performed an a DRON-2-type diffractometer using CrK_{α} radiation.

The dielectric permitivity and loss tangent were obtained in the temperature range 300-500 K at 1 KHz using a digital automatic bridge KEITHLEY 3300 LCZ.

The magnetic susceptibility measurements were performed using a Faraday-type balance in the temperature range 80-300 K.

RESULTS AND DISCUSSION

The X-ray diffraction patterns from the PFN samples were indexed (Fig. 1). The diffraction patterns confirm an orthorhombic structure having the cell parameters a = 5.85 Å ; b = 7.95 Å; c = 6.64 Å and $\beta = 90^{o}$. The intense diffraction line are structure lines which can be indexed as the single perovskite structure. No lines of lower intensity of superstructure were observed. This fact indicate the absence of ordering of the ions in octahedral positions and PFN may be considered as a disordered solid solution. The other lines could not be indexed.

The temperature dependence of dielectric permitivity and loss tangent for PFN compound is shown in Fig. 2. From these dependences my be concluded that PFN exhibit a difuse phase transition in the temperature range 110 – 140^{o}C, which may be a ferroelectric transition in good agreement with results obtained by Smolenskii et al. on powder Pb_2FeNbO_6 [3]. No anomaly of loss tangent was observed.

Due to the presence of the Fe ions in octahedral positions of PFN it is possible that this compound to be also antiferromagnetic [4].

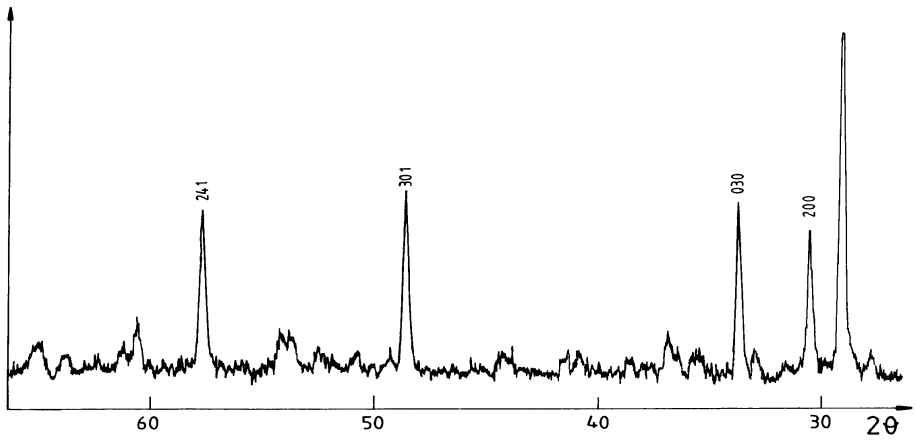

Fig. 1. The X-ray diffraction patterns for PFN sample.

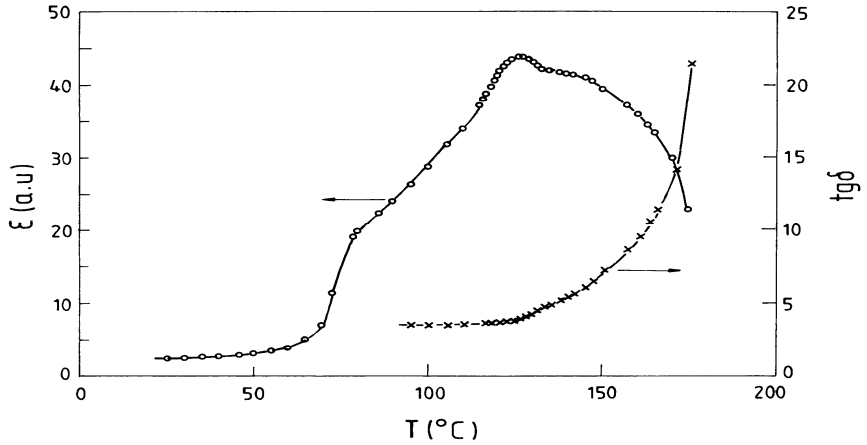

Fig. 2. The temperature dependence of the dielectric constant and loss tangent for PFN sample.

The temperature dependence of the reciprocal magnetic susceptibility χ^{-1} of PFN sample follows a Curie-Weiss behaviour (Fig. 3). These data suggest the presence of the superexchange-magnetic interactions between iron ions. From the molar Curie constant the atomic effective magnetic moment was determined: μ_{eff} = (5.54 ± 0.01) μ_B. This value is situated between magnetic moment of the free Fe^{3+} ion state ($\mu_{Fe^{3+}}$ = 5.92 μ_B) and that of the free Fe^{2+} ion state ($\mu_{Fe^{2+}}$ = 4.90 μ_B). From

these data we have obtained in first approximation the concentration of Fe^{3+}: 61 % and Fe^{2+}: 39 %.

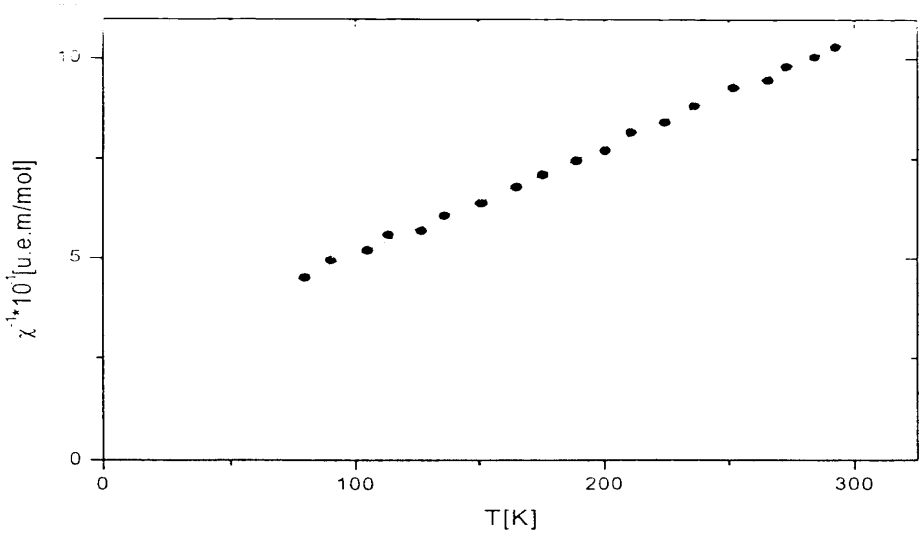

Fig. 3. The temperature dependence of reciprocal magnetic susceptibility for PFN sample.

From the temperature dependence of χ^{-1} we have also determined the paramagnetic Curie temperature θ_p = -88 K which confirm antiferromagnetic behaviour of Pb_2FeNbO_6 compound. On the other hand, value of θ_p reported by Bokov et al. [4] (θ_p = -520 K) differ by that obtained in our measurements. This discrepancy may be due to the different magnetic susceptibility method measurements, or to the accuracy in θ_p determination in Bokov's experiences.

CONCLUSIONS

The X-ray diffraction measurements performed on Pb_2FeNbO_6 samples indicate the absence of ordering of the ions in octahedral positions.

From temperature dependence of the dielectric permitivity it may be concluded that PFN undergo a difuse ferroelectric phase transition in the temperature range 110 – 140^{o}C.

On the other hand, the temperature dependence of reciprocal magnetic susceptibility confirm antiferromagnetic behaviour of PFN due to the presence of the Fe ions in octahedral positions.

REFERENCES

1. T.R. Shrout, A. Hallyial, Am.Ceram.Soc.Bull. 66, 704 (1987).
2. F.S. Galasso, Perovskites and high T_c-superconductors (Gordon and Breach, New-York, 1990)
3. G.A. Smolenskii, A.I. Agranovskaya, S.N. Popov, V.A. Isupov, Sov.Phys.Tech. Phys. 3, 1981 (1958).
4. V.A. Bokov, I.E. Milnikova, G.A. Smolenskii, JETF, 42, 643 (1962).

STUDIA UNIVERSITATIS BABEŞ-BOLYAI, PHYSICA, XLVI, 2, 2001

SIMPLE IONIZATION OF MOLECULAR HYDROGEN BY POSITRON AND ELECTRON IMPACT

SZ. NAGY[1], L. NAGY[1] AND R. I. CAMPEANU[2]

ABSTRACT. In this paper we have applied a formulation for calculating the cross sections within the distorted wave Born approximations for molecular H_2 ionization using the partial-wave expansion method. In addition, Heitler-London-type molecular wavefunctions are used for the description of the initial state. In the case of the e^- projectile, the electron exchange in the transition matrix element has been neglected. The results are compared to the experimental data of Fromme et al [1] and Moxom et al [2] and to other theoretical predictions.

Introduction

The theoretical study of the ionization process in collision of positrons and electrons with atoms has been the subject of several theoretical works in recent years. But little was done on molecular targets.

Measurements on molecular hydrogen have been made by Fromme et al [1] and Knudsen et al [3]. They have used coincident techniques combined with time of flight measurements to determine the cross sections for direct ionization. In 1996 Moxom et al [2] have reported similar ionization cross sections. They eliminated the background caused by random extraction of ions, present in the original work of Knudsen et al [3]. Theoretical calculations have been made by Chen et al [4-5] and Campeanu et al [6] etc.

In this work we have applied the distorted wave Born approximation method (DWBA) which is largely used to determine the T matrix elements in ionization collisions within the intermediate collision velocity region.

[1] Faculty of Physics, Babes-Bolyai University, 3400 Cluj Napoca , Romania
[2] York University, Toronto, Canada.

By using this model we have calculated total cross sections for e^+ and e^- projectiles on H_2 target. In the case of the e^- projectile the electron exchange was neglected. Our results are compared to experiments and to theoretical predictions. To describe the initial bound state of the H_2 molecule we have used simple Heitler-London type orbitals. We have used in total six model representations of the final state. We have used CCA-like and CPE-like (Coulomb wave-plane wave description with effective screening) models. The major difference betwen CCA-like and CPE-like models is that CCA does not include any screening of the residual ion, while the CPE-like models consider screening by the slower outgoing particle.

Theory

The total cross section can be written as:

$$\int_0^E \sigma(E_e) dE_e. \tag{1}$$

where $E_e = E - I$ is the maximum energy of the scattered particle and I is the ionization potential.
Using partial-wave expansions and performing the angular integrals for the differential cross sections $\sigma(E_e)$ in units of πa_0^2 one can obtain

$$\sigma(E_i) = \frac{16}{\pi E_i} \int_0^E dE_e \sum_{l_i l_b l_e l_f L} (2L+1) \mid f_{l_i l_b l_e l_f L}(E_e) \mid^2 . \tag{2}$$

where l_i and l_f are the projectile orbital angular momentum quantum numbers in the incident and final channels respectively, l_e is the corresponding quantum number of the ejected electron and L is the total orbital angular momentum. $f_{l_i l_b l_e l_f L}(E_e)$ is the ionization amplitude which can be written as:

$$f_{l_i l_b l_e l_f L}(E_e) = -Z \sum_{\lambda} f_{\lambda}(l_i l_b l_e l_f L) \int dr_1 dr_2 y_f(r_1) y_e(r_2) \frac{r_<^{\lambda}}{r_>^{\lambda+1}} y_i(r_1) y_b(r_2). \tag{3}$$

where f_{λ} is an angular factor given by:

$$f_{\lambda}(l_i l_b l_e l_f L) = (-1)^{l_b + l_e - L} \sqrt{(2l_i+1)(2l_f+1)(2l_b+1)(2l_e+1)(2L+1)}$$

$$\begin{pmatrix} l_i & l_f & \lambda \\ 0 & 0 & 0 \end{pmatrix}\begin{pmatrix} l_b & l_e & \lambda \\ 0 & 0 & 0 \end{pmatrix}\begin{Bmatrix} l_b & l_i & L \\ l_f & l_e & \lambda \end{Bmatrix}. \tag{4}$$

The functions $y(r)$ are radial wavefunctions**.**

Models

As in a previous paper [8], the initial ground state of the H_2 molecule was described with the Heitler-London-type wave functions of Shull and Ebbing [9]:

$$\Psi(r_1, r_2) = N[\varphi_a(r_1)\varphi_b(r_2) + \varphi_b(r_1)\varphi_a(r_2)]. \tag{5}$$

where φ is a hydrogen-like wavefunction of s type.

The sum of φ_a and φ_b with the same radial coordinates is expanded into a Legendre series:

$$\varphi_a(r_2) + \varphi_b(r_2) = \sum_{l_b} C_{l_b}(r_2, R_0) P_{l_b}(\cos\omega). \tag{6}$$

The expansion coefficients are defined as:

$$C_{l_b}(r_2, R_0) = \frac{2l_b + 1}{2}\int_{-1}^{+1} dx P_{l_b}(x)\left\{\exp\left[-\xi\left(r_2^2 + \frac{R_0^2}{4} - r_2 R_0 x\right)^{\frac{1}{2}}\right] + \exp\left[\xi\left(r_2^2 + \frac{R_0^2}{4} + r_2 R_0 x\right)^{\frac{1}{2}}\right]\right\} \tag{7}$$

where $\zeta = 1.165$ and $R_0 = 1.42$. We have made calculations for $l_b = 0$ which corresponds to the monopole contribution and $l_b = 2$ for the quadrupole contribution. The radial continuum wavefunctions employed in integral (3) were obtained numerically by solving the Schrödinger equation:

$$\left[\frac{d^2}{dr^2} - \frac{l(l+1)}{r^2} - 2V_x(r)\right] y_x(r) = E_x y_x(r). \tag{8}$$

where $x \equiv i, f$ or e.

The choice of the incident projectile wave function $y_i(r)$ is not too important. We have used simple plane waves and Coulomb waves. We have solved equation (8) for six different sets of potentials in order to obtain the continuum state wave functions of the particles involved. In Table 1. we give a complete list of potentials used in the case of CCA-like approximations. The CCA model corresponds to the assumption that both particles, the scattered positron and the ejected electron, move in the field of the residual ion. This picture is inaccurate as it does not allow for the screening of H_2^+ by the slower outgoing particle [7].

Table 1.
Potentials used in the representation of the incident and outgoing waves in the case of the CCA-like models.

Approxi-mation	E_i	E_f	E_e
CCA	0	$1/r_1$	$-1/r_2$
CCA*	0	$2/r_1$-V(r)	$-2/r_2$+V(r)
CCA**	$2/r_1$-V(r)	$2/r_1$-V(r)	$-1/r_2$+V(r)

The picture of the CPE model is that when the ejected electron moves outwards more slowly than the outgoing e^+. The e^- "sees" the positive +1 charge of the residual ion so that it leads to the plane-wave motion of the outgoing e^+; when the ejected e^- moves faster than the outgoing e^+ , the positron 'sees' the positive +1 charge instead and screens the residual ion, which causes the ejected electron to "see" a +2 charge.

The most sophisticated model seems to be that of [10], called CPE4. It assumes that the ejected electron moves always in the combined field of the residual ion and the scattered positron. Table 2. presents the complete list of the potentials used in the case of CPE-like models.

Table 2.
Potentials used in the representation of the incident and outgoing waves in the case of the CPE-like models.

Approxi-mation	$E_e<E_f$			$E_e>E_f$		
	V_i	V_f	V_e	V_i	V_f	V_e
CPE	0	0	$-1/r_2$	0	$1/r_1$	$-2/r_2$
CPE*	0	0	$-1/r_2$+V(r)	0	0	$-1/r_2$+V(r)
CPE4	0	0	$-(1-E_e/E_{ef})/r_2$	0	$1/r_1$	$-2/r_2$

In Tables 1. and 2. $V(r)$ denotes the static potential of the electron cloud:

$$V(r) = \int dr_3 \frac{|\Psi(r_3)|^2}{|\vec{r}_2 - \vec{r}_3|}. \tag{9}$$

and $E_{ef} = E_e + E_f - 2\sqrt{E_e E_f}$.

Results and discussion

For the calculation of cross sections we have used Eq. 2. In the case of the electron projectile we have neglected the electron exchange. The continuum wavefunctions were determined by solving numerically Eq. 8. by using Numerov's method. The double integral from Eq. 3 was evalutated by using Simpson's rule. The energy integral in equation 2 was evaluated by using a Gauss-Legendre quadrature with six nodes. The summation after partial waves was done up to the values $l_e = 7$, $l_i = 15$ and l_f was calculated from the triangle rule involving l_i and l_e. The partial-wave series have been found convergent, and have been calculated up to a precision of 1%.

In Figure 1. we have plotted our results obtained by using CCA-like approximations, and compared them to the experimental results.

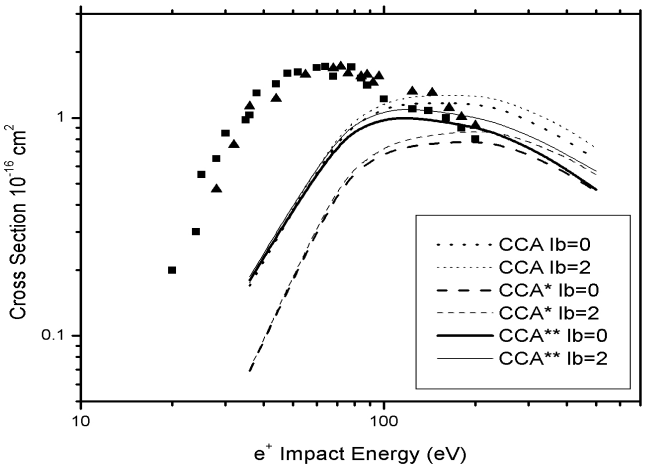

Fig. 1. Calculated cross sections for the ionization of the hydrogen molecule by positron impact using the CCA model compated with the experimental data represented by sqares [1] and triangles [2]. The contribution of the l_b=0 spherical component is shown separately.

In Figure 2. we have plotted our results obtained by using CPE-like approximations, and compared them to the experimental results. Comparing the two classes of approximations we can conclude that the CCA models strongly underestimate the cross sections for lower collisions energies. The CPE results are closer to the experimental data, but there exists an overestimation of the cross section at larger projectile energies.

The best results are obtained with the CPE* model, where the screening is taken into account correctly.

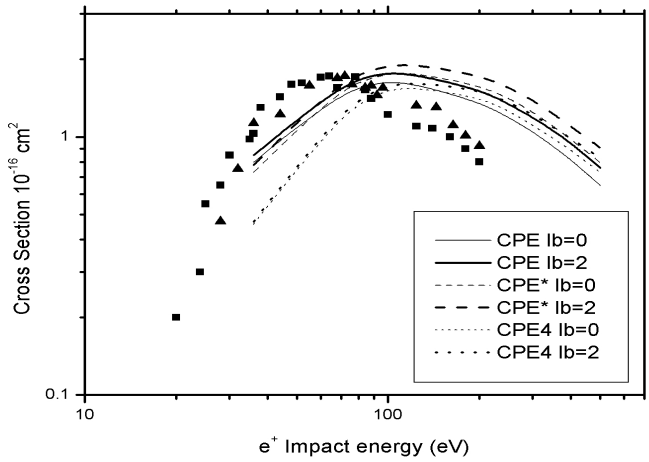

Fig. 2. Same as Figure 1, but using the CPE model.

Figure 3 compares our CCA and CPE results with the experimental data and other theoretical results. Here we observe that the use of two-center molecular wave fuctions instead of spherically averaged ones does not improve the results. Probably to be consistant, the continuum wavefunctions should be calculated also in the nonspherical molecular field.

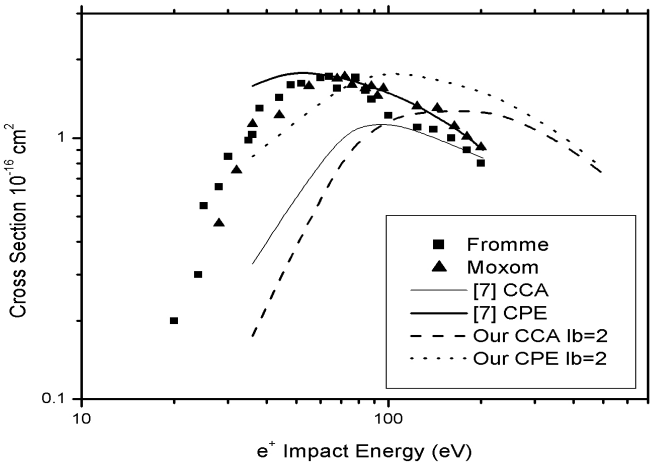

Fig. 3. Comparison of the results obtained using different approximations with the experimental data [1,2] and other theoretical cross sections.

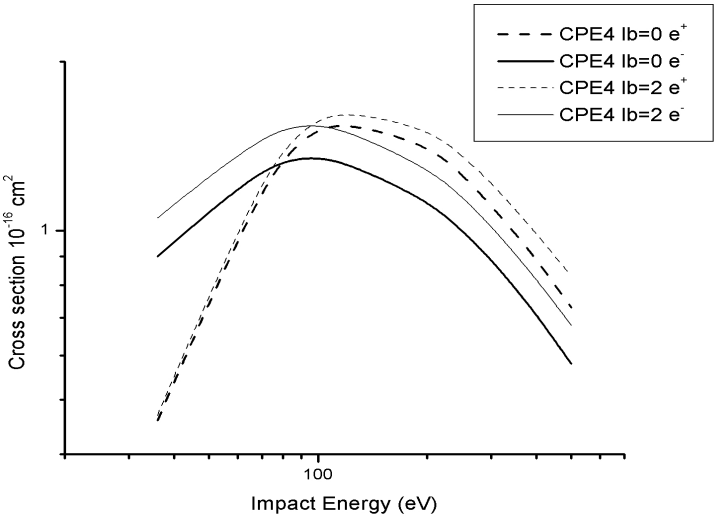

Fig. 4. Ionization cross sections for the hydrogen molecules by positron and electron impact.

Figure 4 compares our CPE4 results obtained for e^+ and e^- projectiles. Here we can observe the projectile charge effect in the ionization of the H_2 molecule. At low projectile energies cross sections for electons are higher, while for energies above 100 eV the cross sections for positrons become higher.

Conclusions

Our work has clearly estabilished the important role played by the screening effects in the final state of the ionising system.

Our results show that the CPE-like models are better then the CCA approximation. The CCA-like models are less accurate as it was predicted by Campeanu et al [6]. The small discrepancy between theory and experiment may somehow be due to the nature of the wavefunction used. In future we intend to improve our calculations by using other type of wavefunctions for the final state.

REFERENCES

1. D., Fromme, G., Kruse, W. Raith and G.J. Sinapius, Phys. B: At. Mol. Opt. Phys. 21 (1998) L261.
2. J. Moxom, P. Ashley and G. Laricchia , Can. J. Phys. 74 (1996) 367.
3. H. Knudsen, L. Brun-Nielsen, M. Charlton and M.R.J. Poulsen, Phys. B: At. Mol. Opt. Phys. 23 (1990) 3955.
4. Xiao Xi Chen, Ji Chen and Jiyun Kuang, J.Phys. B: At. Mol. Opt. Phys. 25 (1992) 5489-5494.
5. Xiao Xi Chen, Ji Chen, Phys.Rev. A 46 No. 11 (1992).
6. R.I. Câmpeanu, J.W. Darewych and A.D. Stauffer, J.Phys. B: At. Mol. Phys. 30 (1997) 5033-5041.
7. R.I. Câmpeanu, R.P. McEachran and A.D. Stauffer, J.Phys. B: At. Mol. Phys. 20 (1987) 1635-1643.
8. L. Nagy, L. Vegh, Phys.Rev. A 46, 284 (1992).
9. H. Shull, D. Ebbing, J. Chem . Phys. 28, 866 (1958).
10. R. I. Câmpeanu, R. P. McEachran, A.D. Stauffer, *Positron Impact Ionization of Hydrogen and Noble Gases*, to be published in Canadian Journal of Physics (2001).

STUDIA UNIVERSITATIS BABEŞ-BOLYAI, PHYSICA, XLVI, 2, 2001

CORRELATION COEFFICIENTS FOR INVESTIGATION OF HEMODYNAMICS BY DOPPLER EFFECT

V. SIMON, M. BICHIS, T. SUTEU*

Babes-Bolyai University, Faculty of Physics,
3400 Cluj-Napoca, Romania
**University of Medicine and Pharmacy, Medical Clinic III,*
3400 Cluj-Napoca, Romania

ABSTRACT. The correlation coefficients are introduced in order to appreciate the functional type of the thyroid gland with a higher accuracy than allowed by pulsatility and resistivity indices usually used in ultrasonography. The correlation coefficients are the ratios between the average velocity obtained for the investigated patients and the normal value of average velocity. For the investigated cases they are ranging between 0.92 and 0.58 in hypothyroidism and between 1.1 and 1.36 in hyperthyroidism.

Introduction

Ultrasonography is the most commonly used primary method of medical investigation among the imiging techniques [1]. The ultrasonic exploration of thyroid gland is based on the analyse of the data obtained by Doppler effect due to its pronounced vascularisation [2]. This method is commonly used to appreciate the volume and ecogenities of thyroid gland [3-5]. Doppler echography allows the computation of physical data as maximal systolic and minimal diastolic velocities which reflect the pulsatility and implicitly the resistivity in the dynamics of sanguine circuit. It is expected to have different values of pulsatility and resistivity indices depending on the thyroid gland metabolism [6].

This study aims to establish correlation coefficients for the sanguine dynamics in the thyroid gland which could evidence the dysfunctions better than the pulsatility and resistivity indices as is imposed especially in the case of hypo function.

Experimental

The ultrasonography analyses were carried out on 180 patients belonging to four age classes starting with the age of 16. For each type of function (normal, hyper and hypo) sixty patients were explored. The measurements were performed on Doppler and Powerangio (Acuson 2020, Logiq 500) equipments. The equipments were identically calibrated in all explorations in order to avoid differences of experimental parameters.

Results and discussion

Doppler echography allows determinating the maximal systolic and minimal diastolic velocities which characterize the pulsatility respectively the resistivity in the dynamics of sanguine circuit [6]. The pulsatility index is defined by the expression:

$$PI = 2(V-v)/(V+v)$$

and the resistivity index is defined as:

$$RI = 1-v/V$$

where V is the maximal systolic velocitiy and v the minimal diastolic velocity. The experimental results obtained for the investigated male (M) and female (F) patients are summarized in Table 1 according to age class and type of function. For the normal function one obtained $PI = 1 \pm 0.03$ and $RI \approx 0.67$, for hyperfunction $PI \approx 0.7$ and $RI \approx 0.52$ while for hypo function $PI \approx 0.95$ and $RI \approx 0.64$. The inspection of these data indicate very low changes both for PI and RI for hypo function relative to the normal function. Therefore we analyzed the values recorded for maximal systolic and minimal diastolic velocities. Figure 1 shows the results obtained for the normal function. Similar dependences are obtained both for hyper and hypo function.

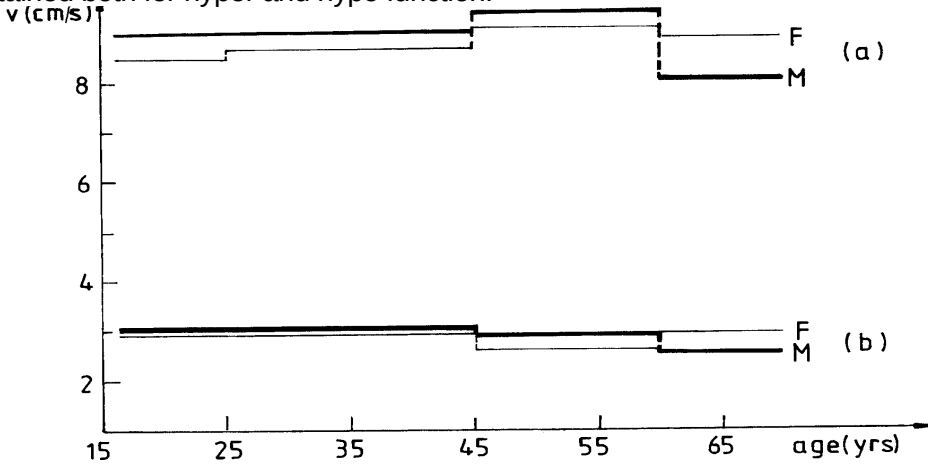

Fig.1. Maximal systolic (a) and minimal diastolic (b) velocities in case of normal function.

Table 1.

Pulsatility and resistivity indices

Age class a (yrs)	M		F		Function
	PI	RI	PI	RI	
16 ≤ a ≤ 25	0,99	0,66	0,98	0,66	normal
	0,68	0,50	0,70	0,52	hyper
	0,92	0,63	0,92	0,63	hypo
26 ≤ a ≤4 5	0,99	0,66	1,00	0,67	normal
	0,78	0,56	0,70	0,54	hyper
	0,95	0,64	0,95	0,64	hypo
46 ≤ a ≤ 60	1,06	0,69	1,03	0,68	normal
	_	_	0,76	0,55	hyper
	0,95	0,60	0,99	0,61	hypo
a > 60	1,06	0,69	1,02	0,67	normal
	_	_	0,71	0,52	hyper
	0,98	0,66	1,03	0,68	hypo

The information is evidently differentiated if we consider the average value between maximal systolic and minimal diastolic velocities as can be seen from Figure 2. Taking into account this observation, we used these dependences to find the correlation coefficients, k, (Table 2) for hyper and hypo function by normalyzing the average velocities to the values corresponding to the undisturbed function. The correlation coefficients have obviously the value 1 in case of normal function. One may observe a much larger range ($0.58 \leq k \leq 1$ for hypothyroidism and $1 \leq k \leq 1{,}36$ for hyperthyroidism) in comparison with the ranges of PI and RI (Table 1).

Table 2

Correlation coefficients for hypo and hyperfunction.

Function	Age class a (yrs)							
	16 ≤ a ≤ 25		26 ≤ a ≤ 45		46 ≤ a ≤ 60		a > 60	
	M	F	M	F	M	F	M	F
	k							
hypo	0.68	0.78	0.78	0.77	0.60	0.58	0.92	0.72
hyper	1.23	1.36	1.20	1.27	-	1.10	-	1.28

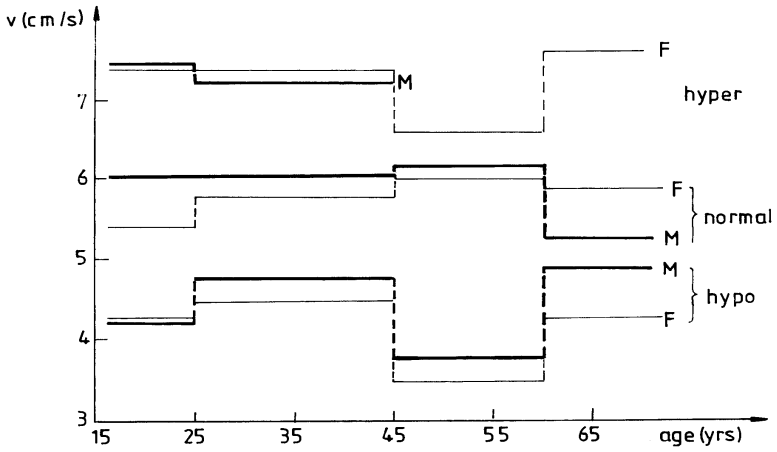

Fig.2. Average velocities for different types of function.

These coefficients enable an easier evaluation of thyroid gland disfunctions particularly in the cases of hypothyroidism for which the pulsatility and resistivity indices are very close to those obtained for the patients with normal function of the thyroid gland.

Conclusion

The correlation coefficients proposed for characterization of sanguine dynamics of thyroid gland are determined using the average values of maximal systolic and minimal diastolic velocities delivered by Doppler effect in ultrasonographical examinations. The correlation coefficients are ranging in a larger domain than the pulsatility and resistivity indices and allow a better indication of the drift from the normal values especially in hypo function cases. On the basis of the preliminary data obtained in this study one may consider that the analyses of correlation coefficients may well offer a useful reliable aid in the effort to diagnose the disfunction of the thyroid gland.

REFERENCES

1. S.J. Abramson, Radiol. Clin. North Am., 35, 6, 1415 (1997)
2. G. Argalia, U. Mignosi, F. Lucarelli, P.P. Morosini, V. Aglieri, G. Giseppetti, Radiol. Med., 93, 1-2, 61 (1997)

3. G. Messina, N. Viceconti, B. Trinti, Recent Progr. Med., 88, 11, 513 (1997)
4. G. Badea, R. Badea, A. Valeanu, P. Mircea, S. Dudea, Bazele ecografiei clinice, Ed. Medicala, Bucuresti, 1994.
5. C. Gervan, I.Duncea, L. Gozariu, Rev. Rom. Ultrasonogr., 2, 1, 45 (2000)
6. M. Rieu, A. Raynaud, A. Richard, S. Laplanche, B. Sambor, J.L. Berrod, Clinical Endocrinol., 41, 667 (1994)

STUDIA UNIVERSITATIS BABEŞ-BOLYAI, PHYSICA, XLVI, 2, 2001

DISORDER AND MAGNETIC FLUCTUATIONS IN NON-HOMOGENEOUS HIGH TEMPERATURE SUPERCONDUCTORS

I. GROSU[1], C. ACHIM[1]

ABSTRACT. The effect of disorder, introduced by non-magnetic impurities, and magnetic fluctuations, is considered in connection with the occurrence of the superconducting state in a non-homogeneous high temperature superconductor. Disorder and non-homogeneities affect the pair-weakening parameter and reduces drastically the critical temperature.

Introduction

Experimental data on high-temperature superconductors (HTS) doped with non-magnetic impurities, such as Zn [1], show a decrease in critical temperature T_c with increase in concentration of impurities which is not of the Abrikosov-Gorkov type. This is one of the most important differences between HTS and classical BCS superconductors. The non-magnetic impurities have a strong destructive effect on critical temperature. This effect is in contradiction with Anderson's theorem which states that a small amount of non-magnetic impurities, randomly distributed, have no effect on the BCS superconducting state. Magnetic measurements on HTS [2] showed the existence of magnetic correlations in both, pure and doped HTS. A realistic theoretical model must take into consideration these effects, in order to explain the drastically reduced critical temperatures in copper oxides doped with non-magnetic impurities.

Model

In the following we will consider that in HTS the superconducting state appears due to a pairing mechanism characterized by an attractive coupling factor λ. We consider that λ is not affected by non-magnetic

[1] Department of Theoretical Physics, University of Cluj, 3400 Cluj, Romania

impurities that are randomly distributed. Neglecting the Coulomb repulsion, the critical temperature is (in the weak coupling limit) [3]:

$$T_c \sim exp\{-\frac{1}{\lambda}\} \tag{1}$$

In the presence of magnetic fluctuations, the critical temperature becomes [4]:

$$T_c \sim exp\{-\frac{1+\lambda+\lambda_m}{\lambda-\lambda_m}\} \tag{2}$$

Here λ_m is the pair-weakening parameter given by:

$$\lambda_m = 2\int_0^{z_c} \frac{dz}{z} g_m(z) \tag{3}$$

z_c is a frequency cut-off, and the kernel $g_m(z)$ is:

$$g_m(z) = \frac{N(0)}{2} \frac{1}{p_F^2} \int_0^{2q_c} qdq[-\frac{1}{\pi} Im\{t(q,z)\}] . \tag{4}$$

$N(0)$ – is the electron density of states, p_F – the Fermi momentum, q_c – a momentum cut-off, and $t(q,z)$ – is the "t"-matrix:

$$t(q,z) = -U^2 \chi_{RPA}(q,z) = -U^2 \frac{\chi(q,z)}{1-U\chi(q,z)} \tag{5}$$

U- is the Hubbard repulsion, and $\chi(q,z)$ is the dynamical susceptibility in the absence of interactions. In the presence of disorder, when $z\tau << 1$, (τ-the scattering time), and $p_F l << 1$, (l- the mean free path), electrons behaves diffusively, and $\chi(q,z)$ has a hydrodynamic form [5]. In the presence of non-homogeneities (non-diffusive spin islands), the diffusive response can be model by a modified susceptibility, given by [6]:

$$\chi(q,z) = N(0) \frac{Dq^2}{Dq^2 - iz - z^2\tau_0} \tag{6}$$

Here *D*- is the diffusion coefficient ($D = v_F^2 \tau / 3$- in three dimensions), and τ_0 is a phenomenological delay time in the response of the system, due to the presence of non-diffusive spin islands. Using eqs.(5) and (6), the imaginary part of the "t"-matrix is:

$$Imt(q,z) = -U^2 N(0) Dq^2 \frac{z}{\{[1-UN(0)]Dq^2 - z^2\tau_0\}^2 + z^2}) \quad (7)$$

With (7) and (4), the pair-weakening parameter λ_m becomes:

$$\lambda_m = \frac{[UN(0)]^2}{\pi} \int_0^{z_c} dz \int_0^{2q_c} \frac{dqq}{p_F^2} \cdot \frac{Dq^2}{z^2 + \{[1-UN(0)]Dq^2 - z^2\tau_0\}^2} \quad (8)$$

Taking $q_c = 1/\sqrt{D\tau}$, the integrals in (8) are easy evaluated, and :

$$\lambda_m = \frac{3}{8\pi}\left[\frac{UN(0)}{1-UN(0)}\right]^2 \frac{z_c\tau}{(E_F\tau)^2}\left\{\frac{\pi}{4} z_c\tau_0 + \right.$$

$$+ \frac{4[1-UN(0)]}{z_c\tau\sqrt{1-8\frac{\tau_0}{\tau}[1-UN(0)]}} \arctan\left(\frac{z_c\tau\sqrt{1-8\frac{\tau_0}{\tau}[1-UN(0)]}}{4[1-UN(0)]}\right) + \quad (9)$$

$$\left. + \frac{1}{2}\cdot\ln\left[1-8\frac{\tau_0}{\tau}[1-UN(0)] + \left(\frac{4[1-UN(0)^2]}{z_c\tau}\right)^2\right]\right\}$$

In the limit $\tau_0 \to 0$ we reobtain the result given in Ref.[7], where the pair-weakening parameter was calculated using a dynamical susceptibility of the form given in [5]. In the figure we plot the pair-weakening parameter (given by eq.(9)), as a function of τ_0, ($z_c\ \tau_0$),for three different values of the Stoner factor *UN(0)*, a) *UN(0)* = 0.99, b) *UN(0)* = 0.95, *UN(0)* = 0.9.

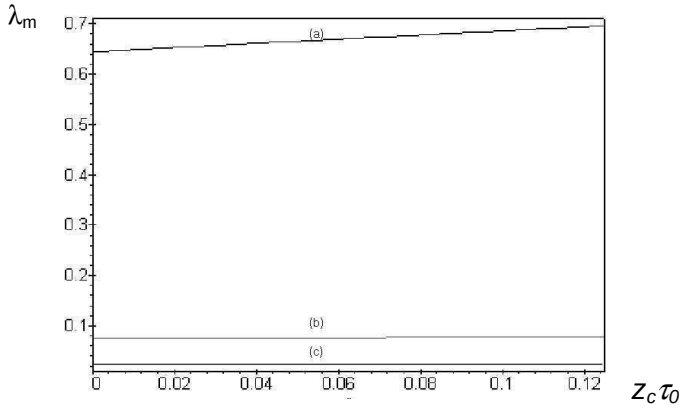

We see that close to the magnetic instability the pair-weakening parameter is strongly enhanced and, as a consequence, the critical temperature, given by eq.(2), decreases drastically. Another effect that increases the pair-weakening parameter is the influence of the delay time τ_0. A larger delay time increases additionally the pair-weakening parameter because these slow modes allow a stronger spin interaction, in a destructive sense for the superconducting state.

Conclusions

We calculated the pair-weakening parameter and the critical temperature for a copper oxide superconductor doped with a small amount of non-magnetic impurities that are randomly distributed. The pair-weakening parameter was determinate using a retarded response function, with a phenomenological delay time τ_0 and in the presence of magnetic correlations, using the Berk-Schrieffer formalism. The aim of this work was to give a simple explanation for the drastically decrease of the critical temperature of copper oxide superconductors in the presence of non-magnetic impurities. We see that this model can give a qualitative explanation for such a behavior. However, other experimental results on HTS lead us to the conclusion that the model can be improved. The first step is to consider "d"-wave superconductivity, instead of "s"-wave superconductivity. Other effect that should be consider is the effect of disorder on Coulomb repulsion. This effect can lead to an additional decrease of the critical temperature [8, 9]. The retarded form of the dynamical susceptibility (model with spin islands) seems to be in agreement with the stripes model for HTS [10, 11].

REFERENCES

1. K. Westerholt, H.J. Wüller, H. Bach, P. Stauche, Phys.Rev.B 39, 11680, (1989).
2. K. Streedhar, P. Ganguly, Phys.Rev.B 41, 371, (1990).
3. J. Bardeen, L.N. Cooper, J.R. Schrieffer, Phys.Rev.108, 1175, (1957).
4. N.F. Berk, J.R. Schrieffer, Phys.Rev.Lett.17, 433, (1966).
5. B.L. Altshuler, A.G. Aronov, D.E. Khmelnitskii, A.I. Larkin, in "Quantum Theory of Solids", I.M.Lifshits ed., p.130, Mir Publishers, Moscow, 1982.
6. L.P. Kadanoff, P.C. Martin, Ann.Phys.24, 419, (1963).

7. I. Grosu, J.Supercond.7, 959, (1994).
8. P.W. Anderson, K.A. Muttalib, T.V. Ramakrishnan, Phys.Rev.B 28, 117, (1983).
9. I. Grosu, T. Veres, M. Crisan, Phys.Rev.B 50, 9404, (1994).
10. N.L. Saini, A. Bianconi, A. Lanzara, J. Avila, M.C. Asensio, S.Tajima, G.D.Gu, N. Koshizuka , cond-mat/9811099.
11. C.N. A van Duin, J. Zaanen, Phys.Rev.Lett.80, 1513, (1998).

STUDIA UNIVERSITATIS BABEŞ-BOLYAI, PHYSICA, XLVI, 2, 2001

TEA N_2-LASER FOR SPECTROSCOPIC GOALS

ZOLTÁN KOVÁCS[1]

ABSTRACT. In our article we present the construction of a thyratron switched Transversal-Electric-Atmospheric (TEA) Nitrogen laser with a capacitive-transfer impulse generator with an impulse jitter kept under control by a very complex electronics suitable for spectroscopic goals performed at the Physics Faculty of the Babe¿-Bolyai University. This article can be helpful also for students in understanding the Nitrogen laser's working process.

The Nitrogen transversal electric atmospheric (TEA) laser is an impulse gaslaser, the wavelength of its radiation being in UV spectra (337,1 nm). Its electrical excitation is transversal on the beam's direction. Inside the laser tube Nitrogen flows at normal pressure which consists its active matter. Other useful information about the Nitrogen lasers can be reached in any other books [1], [2], [3]. The impulse frequency of our laser can be varied between 1 and 25 Hz and its output beam energy does not exceed 10 J. With such a laser can pump a dye laser or produce the fluorescence on organic matter.

The simplest example of this kind of laser can be built easily [5]. But the impulse shape of such a laser will be most noisy. Nitrogen laser at low pressure and for high frequency can also be constructed [7].We planned our laser with devices put at our disposal by the Quantumelectonics and Optics Department of JATE University of Szeged/Hungary and we used a special electronics that allows to produce a very accurate shape of the impulse [6]. A general overview of the latest scheme of our lasers and also all its components is presented in Figure 1.

[1] Babes-Bolyai University, Cluj, Romania.

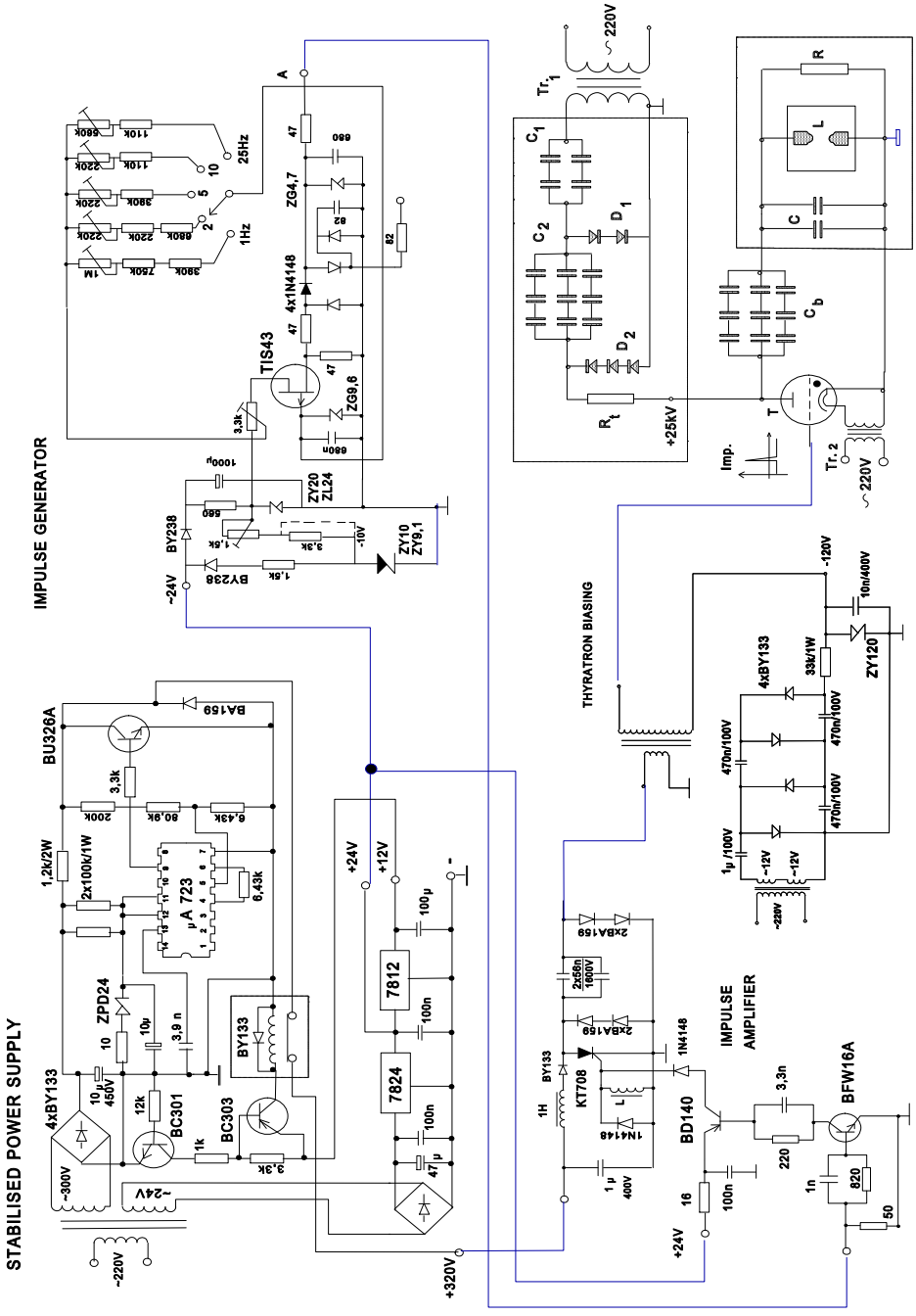
STABILISED POWER SUPPLY
IMPULSE GENERATOR
THYRATRON BIASING
IMPULSE AMPLIFIER
4xBY133
BU326A
BA159
μA 723
ZPD24
BY133
BC301
BC303
7812
7824
+320V
+24V
+12V
-24V
~24V
~300V
~220V
TIS43
4x1N4148
ZG4,7
ZG9,6
ZY20
ZL24
ZY10
ZY9,1
BY238
25Hz
1Hz
KT708
BD140
BFW16A
1N4148
2xBA159
2x56n
1600V
1H
1μ
400V
100μ
100n
47μ
10μ
450V
1,2k/2W
2x100k/1W
200k
80,9k
6,43k
3,3k
12k
1k
3,9 n
10p
10
3,3k
Tr.1
220V
C1
C2
D1
D2
Rt
+25kV
Cb
C
L
R
T
Imp.
Tr.2
4xBY133
33k/1W
ZY120
-120V
10n/400V
470n/100V
1μ /100V
-12V
-28V
1N4148
16
100n
220
3,3n
1n
820
50

Figure 1

High voltage supply

The high voltage supply and the capacitive transfer impulse generator are presented in Figure 2. The AC with 220V is transformed with a high voltage transformer at about 10 kV voltage. Using Barium-titanic capacitors (1nF/12kV) the voltage of 10 kV is transformed in a 25 kV one in two steps. The high voltage diodes used were KC 201 D type for 10 kV.

This high voltage is transferred through the R_t and R resistors to a capacitor bank with 1 nF capacity. When the high power thyratron (ТГИ 500/16 type) is biasing to conduct, the charges of the bank capacitor are transferred to the capacitor C connected in parallel with laser electrodes. Instantaneously is produced a discharge flame between electrodes exciting the Nitrogen and started its lasering. This kind of impulse generator is called capacitor transferring impulse generator.

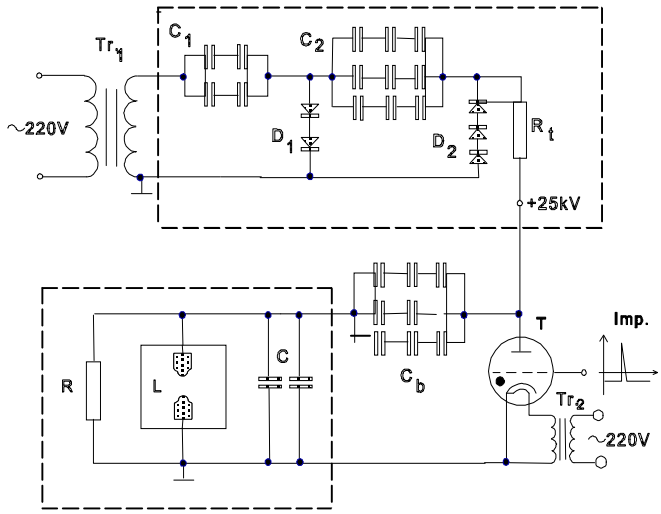

Figure 2

Figure 3 presents the view of the laser tube with Aluminum electrodes. The two parallel connected capacitors are made of printed circuits plates both with 500 pF capacity. The distance between the electrodes can be varied with a micrometer screw. The laser presented below is a perfected one. The earlier type [4] made the high voltage in three steps from a transformer which gave only 5 kV, not enough to excite the gas.

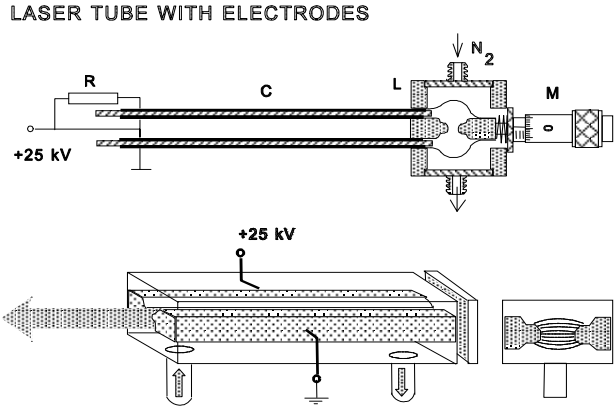

Figure 3

The biasing electronics of thyratron's

A DC of -120 V is constantly applied on the grid of the thyratron, so it is swiched off. It will be switched on under a voltage impulse of +800 V, so its grid will be biasing at about +680 V. This voltage is obtained from an impulse generator whose voltage is transformed in a high voltage with a transformer which gets its voltage from an impulse amplifier. All the voltages necessary to function all units are assured by the stabilized power supply. These four units were projected and built in the Laboratories of the JATE University of Szeged.

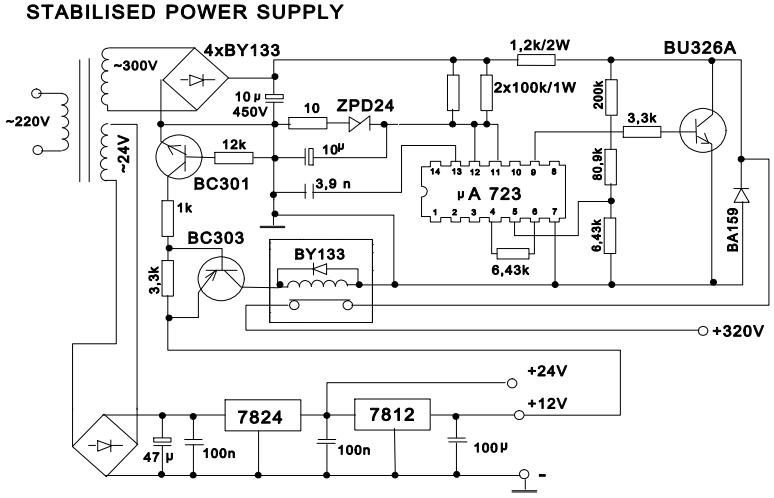

Figure 4

1. The stabilized power supply (Figure 4).

The mains transformer offers two voltages at the same time, 300V and 24 V. Both voltages are rectified with four diodes (BY 133 type) and

filtered with 47 μF capacitors. The stabilization of the voltage is ensured by IC (μA 723 type). Its supply can be in the range of 9.5 and 40 V, in our case being about 24 V made by a Zener diode (ZPD24 type). The 3.9 nF capacitor on the 13th feet of IC assures the overheating protection of the operational amplifier (opamp) of the circuit, while the resistor with 6.43 Ω makes relation between the thermic compensate reference voltage and the noninverting input of the opamp. The output of the integrated circuit (IC) is connected on the BU326A type power transistor. The three resistors' series network (6.43kΩ, 80.9 kΩ and 200kΩ) measured the output voltage, assuring the negative feedback on the compare element of the IC. A second stabilizing process is also realized for the low voltages of 24V and 12V with the 7824 and 7812 devices .

A special task is realized by the transistors BC301 and BC303. Not under current in the collector circuit of the transistor BC303 (when the mains voltage has a value of 0 V) the relay is shut down and the stabilized voltage can reach the impulse amplifier. So, the thyratron is switched on at the moment of 0 V of the mains and the bank capacitor is discharged freely without getting new charges on it. In this way the discharge process is not perturbed and the impulse shape has a good form (the jitter is eliminated). In this manner the transistor BC301 is in conduction state only when the pulsing DC voltage takes its highest value. The collector current of this transistor biasing the BC303 transistor, the relay is switched of during on the conducting period of these transistor. So the impulse amplifier will not be connected while the thyristor KT708 (Figure 1) doesn't conduct.

2. The impulse generator (Figure 5)

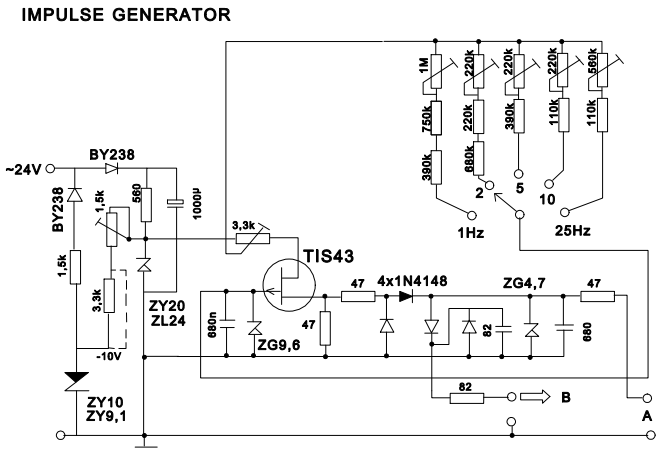

Figure 5

Its function is based on some RC circuits consisted of a 680 nF capacitor in the TIS43 J-FET transistor's grid and a lot of resistors. With

them there can be fixed the time constant of the circuits and also the impulse length. The voltage supply needed for this unit is AC of 24 V. The ZG9.6 and ZG4.7 Zener-diodes ensure the polarization security of junction pn of J-FET transistor, and also limit the external applied triggering voltage in the point A. The transistor conducts while the voltage across the capacitor doesn't exceed a certain value. This time is controlled by the RC time constant of the RC elements. During the time of conducting of the transistor, throughout the diode 1N4148 a current-impulse is going out. While the transistor is shut down, the capacitor discharged itself. So the transistor is prepared to its next working period. The impulse frequency can be selected with a Jexley switcher. The frequency can be fixed with the trimmers at the value of the fractional parts of the mains frequency, namely: 1, 2, 5, 12.5, 25 Hz. The output voltage of impulse generator (4.7 V) is sent to an impulse amplifier unit.

3. The impulse amplifier (Figure 6)

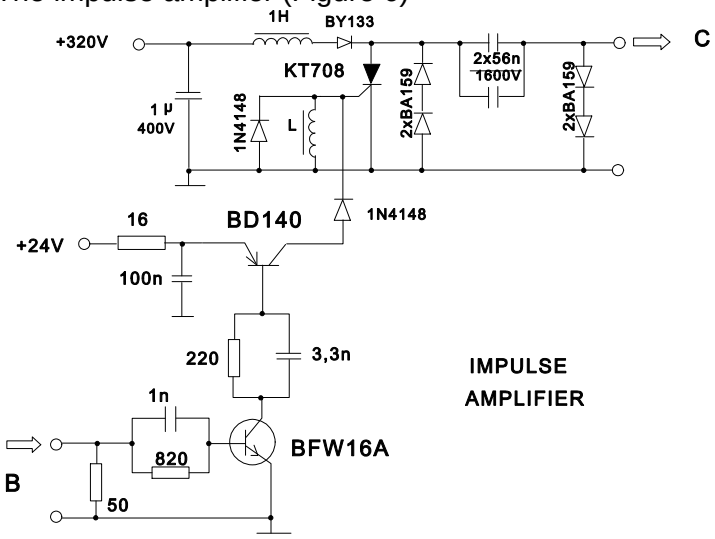

Figure 6

The stabilized DC 320 V charges periodically the 1 µF capacitor connected to the input of the amplifier. The 1 H inductor protects the thyristor KT708 from the peak value of the current, that is not to switch on without the presence of a control-impulse. The same high voltage is applied to the primary coil at the next unit and, through the two diode (BA159), on the two parallel capacitors of 56 nF/1600V. The voltage in the point C is almost 0V. When an input voltage impulse arrives in B point, the base-emitter junction of the high frequency transistor (BFW16A) starts to conduct, and its collector current controls the BD140 transistor. This

happens instantaneously because of the presence of the capacitor with 1 nF in the base circuit of the transistor BFW16A which grows the impulse front slope. The 820 Ω resistor discharges this capacitor during the time the transistor does not conduct.

The role of the 3.3 nF capacitor in parallel with the 220 Ω resistor is the same but for the transistor BD140. The 16 Ω resistor and the 100 nF capacitor represent a low-pass filter circuit which eliminates the perturbation of the circuit in order not to provide the thyristor switch on.

The diode 1N4148 has to take care of the command transistor in the case of breakdown of the thyristor. A coil and a diode make the front shape of the impulse steep.

When the thyristor is switched on it represent a short circuit, and at the output C the voltage of the capacitor with 56 nF appears. The voltage coming from the impulse generator will be amplified in amplitude.

4. The thyratron control unit (Figure 7)

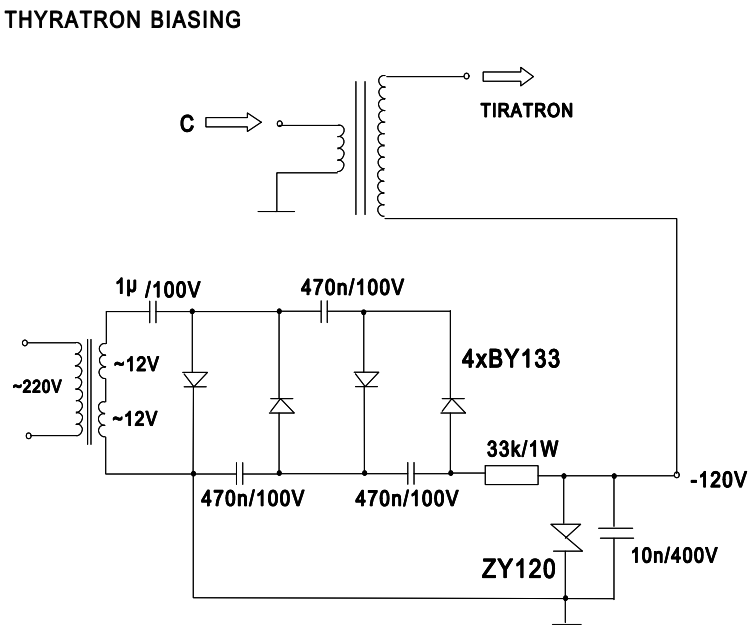

Figure 7

This circuit provides the DC of -120 V for the grid of the thyratron. This voltage is made by a rectifier-multiplier of AC 24 V. It is stabilized with a ZY120 Zener-diode. This value will be overlaid by the hundreds of volts provided with a ferrite core transformer.

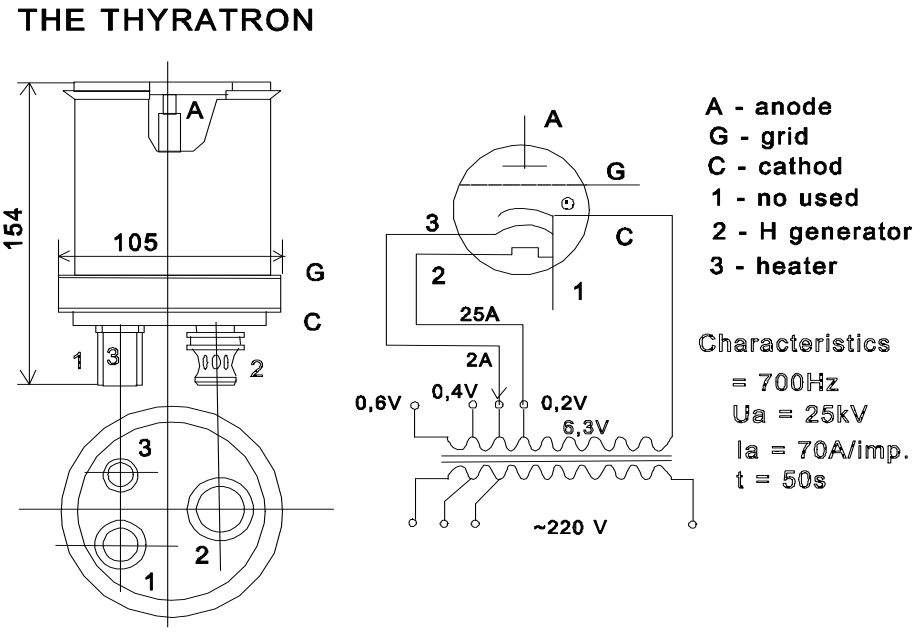

Figure 8

This way the grid of the thyratron will be biasing at about DC +680 V and the quick discharge of the bank capacitor will take place. In Figure 8 the thyratron is presented.The thyratron (ТГ И 500/16 type) is used as a quick switching element in the capacitive-transfer impulse generator circuit. To get a switching time shorter than 40 ns, a thyratron with 5 ns switching time and the large current intensity (500 A) must be used. The heating of the filament is provided by a 25A/6.3V transformer. To generate Hydrogen in thyratron is required a current of 0.2A during 5 minutes. The laser can be switched on only after this heating time. From a Nitrogen tube lead the gas in the laser, the UV spot of the laser beam can be observed on a Photography paper. Using a cylindrical quartz lens we can focus the beam on a dye laser pumping it.

The last picture (Figure 9) shows the constructive scheme of our laser.

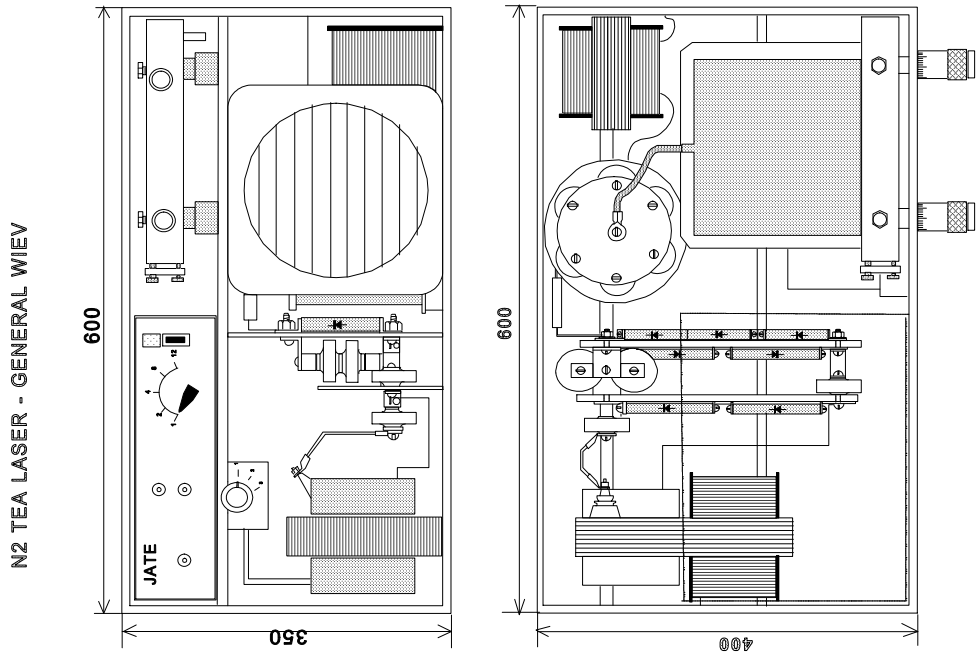

Figure 9

Acknowledgments. We are grateful to professors Mr. Zsolt Bor and Béla Rácz from the Quantumelectronics and Optics Department of Szeged University and also to Sándor Szatmáry and Miklós Molnár from the Physics Department of the same university and to prof. dr. E. T¾taru and conf. dr. T. Iliescu from the Babe¿-Bolyai University of Cluj, Physics Department for their useful help and advice through the years. We are also grateful to conf. dr. S. Anghel and conf. dr. Z. Néda at the same university for their help in preparing this article.

REFERENCES

1. Bor Zsolt, Kovács Gábor, Hebling János, Rácz Béla: *Lézerfizikai kutatások Szegeden. I. Nitrogénlézerek.* Fizikai Szemle. 7 (1978) 257-263.
2. Demtröder, W.: *Laser Spectroscopy.* N.Y. Mc. Graw-Hill. 1978.
3. Hecht, J.: *The Laser Guidebook.* McGraw Hill Book Company. N.Y. (1986).

4. Kovács Zoltán: *Atmoszférikus (N_2-TEA) nitrogénlézer spektroszkópiai mérésekhez.* Műszaki Szemle. II.5-6 (1999) 11-14.

5. Low, K.S.: *Basic Spectroscopy Instrumentation. Nitrogen Laser.* Proceedings of the Winter College on Atomic and Molecular Physics. Kuala Lumpur. (1987)

6. Sánta, I., Rácz, B., Kozma, L. Német, B.: *Investigations of UV TEA N-Lasers.* Acta Physica et Chemica. Szeged XXIV (1978) 395-399.

7. Sánta, I., Kozma, L., Lupkovics, G.: *High Frequency TEA Nitrogen Laser.* JPTE Pécs (1988).

STUDIA UNIVERSITATIS BABEŞ-BOLYAI, PHYSICA, XLVI, 2, 2001

LOWER HYBRID WAVES PROPAGATION IN A MAGNETIC MIRROR CONFINED PLASMA

J. KARÁCSONY[1], K. HORVÁTH[1]

ABSTRACT. Recently, a simple diagnostic method based on lower hybrid waves was proposed to determine electron densities in magnetized plasmas. The diagnostic of the electron cyclotron resonance ion source plasma through these waves needs the stability analysis of magnetic mirror confined plasma. Using the electrostatic dispersion equation for a bi-Maxwellian distribution, the dispersion equation for a loss cone distribution was deduced. Under the experimental conditions corresponding to electron cyclotron resonance ion source plasma, the analysis of this equation indicates that in the spectral domain of the lower hybrid waves, the plasma is stable.

INTRODUCTION

Lower hybrid waves are electrostatic waves with frequency well above the ion cyclotron frequency and at the same time well below the electron cyclotron frequency. They propagate almost perpendicular to the magnetic field lines in magnetically confined plasmas.

Recently [2], a simple diagnostic method based on lower hybrid waves was proposed. This method can be used to determine global average electron densities in magnetized plasmas for which the heat flux to a structure is not prohibitively high so as to be physically destructive. The method is based on the fact that the propagation angle of lower hybrid waves to a magnetic field is a function of electron density. As a result of this it can be used to measure electron density. Tests of the lower hybrid wave. diagnostic were successfully performed in Q machine plasmas. We consider that this diagnostic method can be also applied for ECR plasmas. ECR plasma means the plasma of an electron cyclotron resonance ion

[1] Babes-Bolyai University, Faculty of Physics, 3400 Cluj-Napoca, Romania

source, a high-performance ion source used as accelerator and as atomic physics experimental apparatus. This plasma is created by high frequency electromagnetic field and confined by magnetic mirror fields.

For plasma confined in a magnetic mirror device, the velocity distribution deviates significantly from a Maxwellian. It may be described by a loss cone distribution [3], in which for a given value of $v_{\|}$ those particles with $v_{\perp} < \gamma \cdot v_{\|}$ are absent from the system. ($v_{\perp}$ and $v_{\|}$ are the components of the particle velocity perpendicular and parallel to the external magnetic field, respectively.) The parameter γ characterizing the loss cone distribution is a function of the magnetic mirror ratio, $R = B_{\max} / B_{\min}$.

Rosenbluth and Post [4] have shown that in a nonequilibrium plasma, where the particle distribution function $f(v_{\perp}, v_{\|})$ is vanishing for $v_{\perp} = 0$, it can appear unstable modes of wave propagation. This is the reason that the use of lower hybrid waves as diagnostic tool needs the stability analysis of a mirror confined plasma in the frequency spectrum corresponding to the lower hybrid wave propagation. This is the goal of our paper.

THE "LOSS-CONE" DISTRIBUTION FUNCTION

The velocity distributions considered by us is the one introduced by Dory, Guest and Harris [3] to model the anisotropic velocity distribution of a mirror-confined plasma. For each species of plasma particles the distribution function is defined by a separable function of $v_{\perp}$ and $v_{\|}$, having the form

$$f_{\alpha}^{(j)}(v_{\|}, v_{\perp}) = \frac{1}{(2\pi)^{\frac{3}{2}} w_{\|\alpha} w_{\perp\alpha}^2 j!} \cdot \left(\frac{v_{\perp}^2}{2w_{\perp\alpha}^2} \right)^j \exp\left(-\frac{v_{\|}^2}{2w_{\|\alpha}^2} - \frac{v_{\perp}^2}{2w_{\perp\alpha}^2} \right) \quad (1)$$

where $w_{\perp\alpha}$ and $w_{\|\alpha}$ are the α particle species thermal velocity in the direction perpendicular and parallel to the external magnetic field, respectively. The index j defines the nature of the distribution. j=0 corresponds to an anisotropic bi-Maxwellian distribution, j=1,2,3…. correspond to the loss-cone distributions. In the later cases the distribution function is zero at $v_{\perp} = 0$ and peaked about a nonzero value of $w_{\perp}(2j)^{1/2}$. The comparison of the distribution function (1) with the numerical calculation of Ben Daniel and Allis [5] leads to the conclusion that an

increasing of the mirror ratio R determines a decreasing of the index j. (For R=1.5 corresponds j=2 and R=3.3 corresponds j= 1)

Now, we will write $f_\alpha^{(j)}$ as a product of a function $h(v_\parallel)$ of the parallel velocity component and a function $g(v_\perp)$ of the perpendicular velocity component so that

$$f_\alpha^{(j)}(v_\parallel, v_\perp) = h_\alpha(v_\parallel) \cdot g_\alpha^{(j)}(v_\perp), \tag{2}$$

where

$$h_\alpha(v_\parallel) = \frac{1}{\sqrt{2\pi} w_{\parallel\alpha}} \exp\left(-\frac{v_\parallel^2}{2w_{\parallel\alpha}^2}\right), \tag{3}$$

and:

$$g_\alpha^{(j)}(v_\perp) = \frac{1}{2\pi w_{\perp\alpha}^2 j!}\left(\frac{v_\perp^2}{2w_{\perp\alpha}^2}\right)^j \exp\left(-\frac{v_\perp^2}{2w_{\perp\alpha}^2}\right). \tag{4}$$

Introducing the linear operator

$$L_\alpha^{(j)} = 1 + \frac{w_{\perp\alpha}^2}{j}\frac{\partial}{\partial w_{\perp\alpha}^2}, \tag{5}$$

the $g_\alpha^{(j)}(v_\perp)$ function can be obtained from the $g_\alpha^{(0)}(v_\perp)$ anisotropic bi-Maxwellian distribution function using the recurrence relation:

$$g_\alpha^{(j)}(v_\perp) = L_\alpha^{(j)} g_\alpha^{(j-1)}(v_\perp). \tag{6}$$

under the form:

$$g_\alpha^{(j)}(v_\perp) = \left(1 + \frac{w_{\perp\alpha}^2}{j} \cdot \frac{\partial}{\partial w_{\perp\alpha}^2}\right)\left(1 + \frac{w_{\perp\alpha}^2}{j-1} \cdot \frac{\partial}{\partial w_{\perp\alpha}^2}\right) \cdots \left(1 + w_{\perp\alpha}^2 \frac{\partial}{\partial w_{\perp\alpha}^2}\right) g_\alpha^{(0)}(v_\perp) = \prod_{l=1}^{j} L_\alpha^{(l)} g_\alpha^{(0)}(v_\perp) \tag{7}$$

THE LOSS-CONE DISPERSION EQUATION FOR LOWER HYBRID WAVES

Assuming that the waves are plane, i.e. all perturbed quantities vary as $\exp\left[i\left(\vec{k} \cdot \vec{r} - \omega \cdot t\right)\right]$, we can write the general dispersion equation for longitudinal waves under the form [6]:

$$\varepsilon_{xx}\sin^2\theta+\varepsilon_{zz}\cos^2\theta+2\varepsilon_{xz}\cos\theta\sin\theta=0\,. \tag{8}$$

ε_{pr} (p,r = x,z) are the dielectric tensor elements of the plasma and θ represents the angle between the wave vector $\vec{k}$ and the direction of the external magnetic field $\vec{B}_0$. (One assumes that the wave vector $\vec{k}$ lies in the XOZ-plane and the OZ-axis is oriented parallel to the external magnetic field.)

Now, to benefit by the fact that the conductivity tensor is additive in its components, it is useful to express the dielectric tensor elements with the aid of the conductivity tensor elements, according to the relation [6]

$$\varepsilon_{pr}=\delta_{pr}+\frac{i}{\varepsilon_0\omega}\sigma_{pr}=\delta_{pr}+\frac{i}{\varepsilon_0\omega}\sum_{\alpha}\sigma_{pr}^{(\alpha)}\,. \tag{9}$$

$\sigma_{pr}^{(\alpha)}$ is the contribution to the conductivity tensor element σ_{pr} from plasma particles of type α. $\delta_{pr}=1$ when p=r, otherwise $\delta_{pr}=0$. Using the relation (9), the electrostatic dispersion equation can be written in the form:

$$1+\frac{i}{\varepsilon_0\omega}\sum_{\alpha}\left[\sigma_{xx}^{(\alpha)}\sin^2\theta+\sigma_{zz}^{(\alpha)}\cos^2\theta+2\sigma_{xz}^{(\alpha)}\sin\theta\cos\theta\right]=0\,. \tag{10}$$

Assuming that the α particle distribution function depends only on the parallel and perpendicular components of the particle velocity, ($v_{\|}$ and $v_{\perp}$), the expressions for $\sigma_{pr}^{(\alpha)}$ (p,r = x,z) becomes[6]:

$$\sigma_{pr}^{(\alpha)}=\frac{2\pi\varepsilon_0}{i}\sum_{n=-\infty}^{\infty}\frac{\omega_{p\alpha}^2}{\omega}\left\{\int_0^{\infty}v_{\perp}dv_{\perp}\int_{-\infty}^{\infty}dv_{\|}\left[\left(\frac{\omega-k_{\|}v_{\|}}{v_{\perp}}\cdot\frac{\partial f_{\alpha}}{\partial v_{\perp}}+k_{\|}\frac{\partial f_{\alpha}}{\partial v_{\|}}\right)\frac{Q_{pr}}{\omega-k_{\|}v_{\|}-n\omega_{c\alpha}}-\right.\right.$$
$$\left.\left.-b_{pr}\left(f_{\alpha}+\frac{v_{\|}^2}{v_{\perp}}\cdot\frac{\partial f_{\alpha}}{\partial v_{\perp}}\right)\right]\right\}, \tag{11}$$

where:

$$Q_{xx}=\frac{n^2\omega_{c\alpha}^2}{k_{\perp}^2}j_n^2\,,\quad Q_{zz}=v_{\|}^2j_n^2\qquad\text{and}\qquad Q_{xz}=v_{\|}\frac{n\omega_{c\alpha}}{k_{\perp}}j_n^2\,. \tag{12}$$

The arguments of the Bessel functions j_n are $x_\alpha \equiv k_\perp v_\perp / \omega_{c\alpha}$; $b_{pr} = 1$ when p=r=z , otherwise $b_{pr} = 0$; $\omega_{p\alpha}$ is the plasma frequency and $\omega_{c\alpha}$ is the cyclotron frequency for the α species of particles; f_α is assumed to be normalized to unity ; $k_{\perp(\|)}$ is the component of the wave vector in the direction perpendicular (parallel) to the magnetic field.

Now, if we express the loss-cone distribution function $f_\alpha^{(j)}\left(v_\|, v_\perp\right)$ with the aid of the anisotropic, bi-Maxwellian distribution $f_\alpha^{(0)}\left(v_\|, v_\perp\right)$ (see Eq. (7)), $\sigma_{pr}^{(\alpha)}$ can be written as

$$\sigma_{pr}^{(\alpha)} = \prod_{l=1}^{j} L_\alpha^{(l)} \sigma_{pr}^{(\alpha,M)} , \tag{13}$$

where $\sigma_{pr}^{(\alpha,M)}$ are the conductivity tensor elements for bi-Maxwellian distribution. Inserting the expression (13) into (10), we obtain:

$$1 + \frac{i}{\varepsilon_0 \omega} \sum_\alpha \prod_{l=1}^{j} L_\alpha^{(l)} \left[\sigma_{xx}^{(\alpha,M)} \sin^2\theta + \sigma_{zz}^{(\alpha,M)} \cos^2\theta + 2\sigma_{xz}^{(\alpha,M)} \sin\theta\cos\theta \right] = 0 . \tag{14}$$

The conductivity tensor elements for a bi-Maxwellian distribution were calculated in [7]. The elements needed by us are:

$$\sigma_{xx}^{(\alpha)} = i\varepsilon_0 \frac{\omega_{p\alpha}^2}{\omega} \left\{ 1 - \sum_n n^2 \frac{A_n(\lambda_\alpha)}{\lambda_\alpha} \left[\frac{n\omega_{c\alpha}}{k_z v_\|} Z(s_{n\alpha}) + \frac{T_{\perp\alpha}}{T_{\|\alpha}} Y(s_{n\alpha}) \right] \right\} , \tag{15}$$

$$\sigma_{xz}^{(\alpha)} = -i\varepsilon_0 \frac{\omega_{p\alpha}^2}{\omega} \cdot \frac{T_{\perp\alpha}}{T_{\|\alpha}} tg\theta \sum_n \frac{A_n(\lambda_\alpha)}{\lambda_\alpha} \left[\frac{\omega}{\omega_{c\alpha}} + n\left(\frac{T_{\|\alpha}}{T_{\perp\alpha}} - 1 \right) \right] Y(s_{n\alpha}) , \tag{16}$$

$$\sigma_{zz}^{(\alpha)} = -i\varepsilon_0 \frac{\omega_{p\alpha}^2}{\omega} \cdot \frac{T_{\perp\alpha}}{T_{\|\alpha}} tg^2\theta \sum_n \left(\frac{\omega}{\omega_{c\alpha}} - n \right) \frac{A_n(\lambda_\alpha)}{\lambda_\alpha} \left[\frac{\omega}{\omega_{c\alpha}} + n\left(\frac{T_{\|\alpha}}{T_{\perp\alpha}} - 1 \right) \right] Y(s_{n\alpha}) , \tag{17}$$

where, instead of the function $j_+(s_n)$ used in [7], we introduced the dispersion functions [8]:

$$Z(s_{n\alpha}) = \frac{1}{(2\pi)^{1/2}} \int_{-\infty}^{\infty} dt \frac{\exp(-t^2/2)}{(t - s_{n\alpha})}, \tag{18}$$

$$Y(s_{n\alpha}) = \frac{1}{(2\pi)^{1/2}} \int_{-\infty}^{\infty} dt \frac{t \cdot \exp(-t^2/2)}{t - s_{n\alpha}}, \tag{19}$$

These functions are related to $j_+(s_n)$ by the relations:

$$j_+(s_{n\alpha}) = -s_{n\alpha} Z(s_{n\alpha}), \tag{20}$$

$$j_+(s_{n\alpha}) = 1 - Y(s_{n\alpha}). \tag{21}$$

The argument $s_{n\alpha}$ is defined by:

$$s_{n\alpha} = \frac{\omega - n\omega_{c\alpha}}{k_{\|} w_{\|\alpha}} \tag{22}$$

In Eqs. (15)-(17) we used the notations:

$$A_n(\lambda_\alpha) = \exp(-\lambda_\alpha) I_n(\lambda_\alpha), \tag{23}$$

where $I_n(\lambda_\alpha)$ is the modified Bessel function of the first kind with the argument $\lambda_\alpha = (k_\perp w_\perp / \omega_{c\alpha})^2$ and $T_{\perp(\|)\alpha} = m_\alpha w^2_{\perp(\|)\alpha}$ is the perpendicular (parallel) temperature for the α species of particles.

Inserting the expressions (15)-(17) into Eq. (14) one can write the electrostatic dispersion equation as:

$$D^{(j)}(\vec{k}, \omega) \equiv 1 + \sum_\alpha \frac{\omega_{p\alpha}^2}{k^2 w_{\|\alpha}^2} \left\{ 1 + \sum_{n=-\infty}^{\infty} \prod_{l=1}^{j} L_\alpha^{(l)} \left[A_n(\lambda_\alpha) \left(s_{n\alpha} + \frac{n\omega_{c\alpha}}{k_z w_{\|\alpha}} \frac{T_{\|\alpha}}{T_{\perp\alpha}} \right) \right] Z(s_{n\alpha}) \right\} = 0 . \tag{24}$$

STABILITY ANALYSIS

In order to investigate the above deduced dispersion equation, we follow the usually applied procedure in plasma physics [6]. According to this, when |Imω|<<Reω , the wave frequencies can be calculated from the equation

$$\mathrm{Re}\, D(\vec{k}, \omega) = 0 , \tag{25}$$

and the imaginary part of the frequency from the relation:

$$\operatorname{Im}\omega = -\frac{\operatorname{Im} D\left(\vec{k},\omega\right)}{\partial \operatorname{Re} D\left(\vec{k},\omega\right)/\partial\omega}. \tag{26}$$

$D\left(\vec{k},\omega\right)$ is calculated with ω real, while $\operatorname{Re} D\left(\vec{k},\omega\right)$ and $\operatorname{Im} D\left(\vec{k},\omega\right)$ denotes the real and imaginary part of D, respectively. Eq. (25) describes wave propagation and Eq. (26) gives an explicit expression for Imω.

Taking into account that for lower hybrid waves $\omega_{ci} << \omega << \omega_{ce}$ and $N^2 >> 1$, we can assume that the particle temperatures have little influence on the waves. We will then use the cold plasma approximation in calculating $\operatorname{Re} D\left(\vec{k},\omega\right)$. Under this assumptions the dispersion relation (25) can be written as [6]:

$$\operatorname{Re} D\left(\vec{k},\omega\right) \equiv \varepsilon_1 \sin^2\theta + \varepsilon_3 \cos^2\theta = 0, \tag{27}$$

where:

$$\varepsilon_1 \cong 1 - \frac{\omega_{pi}^2}{\omega^2} + \frac{\omega_{pe}^2}{\omega^2}, \tag{28}$$

$$\varepsilon_3 \cong -\frac{\omega_{pe}^2}{\omega^2}. \tag{29}$$

Solving this equation, we obtain for the wave frequency the expression :

$$\omega^2 = \omega_{LH}^2 + \frac{\omega_{pe}^2\omega_{ce}^2}{\omega_{pe}^2 + \omega_{ce}^2} ctg^2\theta, \tag{30}$$

where:

$$\omega_{LH}^2 = \frac{\omega_{ce}\omega_{ci}}{1 + \omega_{ce}^2/\omega_{pe}^2}, \tag{31}$$

is the lower hybrid frequency [1].

Furthermore, if we neglect the influence of thermal effects on the value of $\partial \operatorname{Re} D/\partial\omega$, we obtain:

$$\frac{\partial}{\partial\omega}\operatorname{Re} D\left(\vec{k},\omega\right) = \frac{2}{\omega^3}\left(\omega_{pi}^2 \sin^2\theta + \omega_{pe}^2 \cos^2\theta\right) \cong \frac{2\omega_{pi}^2}{\omega^3}. \tag{32}$$

Now, by using for the plasma dispersion function $Z(s_{n\alpha})$ the definition [8]

$$Z(s_{n\alpha}) = -\exp\left(-\frac{s_{n\alpha}^2}{2}\right)\left[\int_0^{s_n} e^{\frac{t^2}{2}} dt - i\left(\frac{\pi}{2}\right)^{\frac{1}{2}}\right], \tag{33}$$

we obtain for $\mathrm{Re}D(\vec{k},\omega)$:

$$\mathrm{Im}\, D^{(j)} = \left(\frac{\pi}{2}\right)^{\frac{1}{2}} \sum_{\alpha} \frac{\omega_{p\alpha}^2}{k^2 w_{\|\alpha}^2} \sum_{n} \prod_{l=1}^{j} L_{\alpha}^{(l)} \left[A_n(\lambda_\alpha)\left(s_{n\alpha} + \frac{n\omega_{c\alpha}}{k_z w_{\|\alpha}} \frac{T_{\|\alpha}}{T_{\perp\alpha}} \right)\right] \exp\left(-\frac{s_{n\alpha}^2}{2}\right). \tag{34}$$

For the lower hybrid wave frequency we have $\omega << \omega_{ce}$ and consequently we can neglect in Eq. (34) the exponentially small electron terms, except the n=0 term. For Imω we can then write:

$$\mathrm{Im}\,\omega = -\sqrt{\frac{\pi}{2}}\left\{ \frac{\omega^3}{2k^2 w_{\|e}^2} \cdot \frac{m_i}{m_e} \cdot \prod_{l=1}^{j} L_e^{(l)} A_0(\lambda_e) \frac{\omega}{k_z w_{\|e}} \exp\left(-\frac{\omega^2}{2k_z^2 w_{\|e}^2}\right) + \right.$$
$$\left. + \frac{\omega^3}{2k^2 w_{\|i}^2} \sum_{n=-\infty}^{\infty} \prod_{l=1}^{j} L_i^{(l)} \left[A_n(\lambda_i)\left(s_{ni} + \frac{n\omega_{ci}}{k_z w_{\|i}} \cdot \frac{T_{\|i}}{T_{\perp i}} \right)\right] \exp\left(-\frac{s_{ni}^2}{2}\right)\right\}. \tag{35}$$

If we are interested in lower hybrid waves propagation in an ECR plasma, we must keep in mind that due to the cyclotron heating the electron temperature is well above the ion temperature and presents a strong anisotropy. On the contrary, the ions can be considered to be isothermic and at low temperature [10]. The imaginary part of the frequency is thereby determined as:

$$\mathrm{Im}\,\omega = -\sqrt{\frac{\pi}{2}} \cdot \omega^3 \left\{ \frac{\frac{m_i}{m_e}}{2k^2 w_{\|e}^2} \prod_{l=1}^{j} L_e^{(l)} A_0(\lambda_e) \frac{\omega}{k_z w_{\|e}} \exp\left(-\frac{\omega^2}{2k_z^2 w_{\|e}^2}\right) + \right.$$
$$\left. + \frac{1}{2k^2 w_{\|i}^2} \sum_{n=-\infty}^{\infty} \prod_{l=1}^{j} L_i^{(l)} A_n(\lambda_i) \frac{\omega}{k_z w_{\|i}} \exp\left[-\frac{(\omega - n\omega_{ci})^2}{2k_z^2 w_{\|i}^2}\right]\right\}. \tag{36}$$

The first term in the brackets on the right-hand side represents a positive definite term arising from the electronic Landau damping. For the stability analysis we must examine the sign of the second term. In the following we introduce the notations:

$$C_n^0 = A_n(\lambda) = I_n(\lambda)\exp(-\lambda)\,, \tag{37}$$

and:

$$C_n^j = \prod_{l=1}^{j} L^{(j)} A_n(\lambda)\,. \tag{38}$$

The introduced C_n^j functions satisfy the recurrence formulas:

$$C_n^j = L^{(j)} C_n^{j-1}\,. \tag{39}$$

Now, the imaginary part of the frequency can be written as:

$$\operatorname{Im}\omega = -\sqrt{\frac{\pi}{2}}\cdot\omega^3\left\{\frac{1}{2k^2 w_{\|e}^2}\cdot\frac{m_i}{m_e}\cdot C_0^j(\lambda_e)\frac{\omega}{k_z w_{\|e}}\exp\left(-\frac{\omega^2}{2k_z^2 w_{\|e}^2}\right)+\right.$$

$$\left.+\frac{1}{2k^2 w_{\|i}^2}\sum_{n=-\infty}^{\infty} C_n^j(\lambda_i)\frac{\omega}{k_z w_{\|i}}\exp\left[-\frac{(\omega-n\omega_{ci})^2}{2k_z^2 w_{\|i}^2}\right]\right\}. \tag{40}$$

In most practical cases the mirror ratio in an ECR ion source is between 1,2 and 3. As a result of this it will be enough to examine the sign of the second term when j=1,2,3 and for which the functions are:

$$C_n^1(\lambda) = \left[(1-\lambda)I_n(\lambda) + \lambda I_n'(\lambda)\right]\exp(-\lambda), \tag{41}$$

$$C_n^2(\lambda) = \left[\left(\lambda^2 - 2\lambda + \frac{n^2+2}{2}\right)I_n(\lambda) - \left(\lambda^2 - \frac{3}{2}\lambda\right)I_n'(\lambda)\right]\exp(-\lambda)\,, \tag{42}$$

$$C_n^3(\lambda) = \left[\left(-\frac{2}{3}\lambda^3 + \frac{17}{6}\lambda^2 - \frac{n^2+6}{2}\lambda + n^2 + 1\right)I_n(\lambda) + \right.$$

$$\left.+\left(\frac{2}{3}\lambda^3 - \frac{5}{2}\lambda^2 + \frac{n^2+11}{6}\right)I_n'(\lambda)\right]\exp(-\lambda)\,. \tag{43}$$

These functions were calculated numerically for the harmonic number n up to 10 and found to be all positive. Thus Imω<0,resulting that the plasma is stable.

CONCLUSION

Lower hybrid waves can be used to measure electron densities in magnetized plasmas. The use of these waves to diagnose electron cyclotron resonance ion source plasma needs the stability analysis of magnetic mirror confined plasma. Using general electrostatic dispersion equation for a two-temperature bi-Maxwellian particle distribution, the dispersion equation for a loss cone distribution was deduced. Solving this equation the expression of the imaginary part of the wave frequency for the lower hybrid wave spectral domain was calculated. The analysis of this expression for experimental conditions corresponding to electron cyclotron resonance ion source plasma indicates a stable propagation of the waves. We conclude that the lower hybrid waves can be used for measuring global average density in electron cyclotron resonance ion source plasma.

In order to apply this method we must take into account the existence of the inhomogeneous B-minimum type magnetic field. The procedure can be applied only in the Resonance Zone, because outside of it the confining magnetic field is strongly inhomogeneous. Inside the Resonant Zone the characteristic length of the field inhomogeneity is larger than the wavelength of the lower hybrid waves. However, in this region other methods, e.g. Langmuir probes can not be applied [11].

Acknowledgment. Part of this research was performed during a Domus Hungarica Scientiarium et Artium fellowship. J. Karacsony acknowledges this fellowship and the scientifically motivating atmosphere from Atomki (Hungary, Debrecen).

REFERENCES

1. F.F. Chen, *Introduction to plasma physics and controlled fusion* (Plenum Press, New York, 1990).
2. D.P. Sheehan, *Rev.Sci. Instrum. 69*, 1699 (1998).
3. R.A. Dory, G.E. Guest, E.G. Harris, *Phys. Rev. Lett. 14*, 131 (1965).
4. M.N. Rosenbluth, R.F. Post, *Phys. Fluids 8*, 547 (1965).
5. D.J. Ben Daniel, W.P. Allis, *Plasma Physics 4*, 31 (1962).

6. I.A. Akhiezer, K.N. Stepanov, R.V. Polovin, A.G. Sitenko, *Elektrodinamika Plazmy* (Nauka, Moskva, 1974) p. 212.
7. A.F. Alexandrov, L.S. Bogdankievic, A.A. Ruhadze, *Osnovy Elektrodinamiki Plasmy* (VISC. Scola, Moskva, 1978) p.146.
8. K.M. Watson, S.A. Bludmann, M.N. Rosenbluth, *Phys. Fluids 3*, 741 (1960).
9. S.S.Sazhin, *Ann. Geophys. 9*, 690 (1991).
10. G.D. Shirkov, C. Mühle, G. Musiol, G. Zschornack, *Nucl. Instr. and Meth.* A 302, 1 (1991).
11. L. Kenez, S. Biri, J. Karacsony, A. Valek, T. Nakagawa,K.E. Stiebing, V. Mironov, in press in *Rev.Sci.Instrum.* (2001).